Materials Advances

PAPER

Check for updates

First-principles study of the ground-state properties of ternary borides with the Ru_3B_2X (X = Th, U) type structure: a comparative analysis†

Md. Raihan Islam,[a] Prianka Mondal[a] and Arpon Chakraborty [ID] *[b]

The distinctive structural, mechanical, electrical, and thermophysical characteristics of the hexagonal Ru_3B_2X (X = Th, U) compounds make them appropriate for high-temperature and cutting-edge technological applications. Their ground-state features are investigated in this work using density functional theory (DFT). Ru_3B_2U exhibits higher stability than Ru_3B_2Th, confirming mechanical stability and advantageous formation in both compounds. Both Ru_3B_2Th and Ru_3B_2U show covalent bonding, moderate hardness, and ductility, with Ru_3B_2Th exhibiting better machinability and greater ductility. Metallic behavior and the characteristic Fermi surface features are highlighted by electronic band structure investigation, with Ru_3B_2Th exhibiting increased electronic conductivity. Although both compounds show strong covalent connections, uranium and thorium have distinct effects on bonding. Both compounds have high Debye temperatures and melting points indicating their strong bonding and thermal stability. Between the two compounds, Ru_3B_2Th is preferable for thermal insulation. Optical properties show that these compounds behave in an anisotropic manner and have modest reflectivity, which is compatible with their metallic electronic structure. Due to their high optical reflectivity in the infra-red (IR) region, they are also candidates for IR-shielding applications. This thorough analysis emphasizes their potential for uses demanding robust thermal, mechanical, and optical characteristics.

1. Introduction

Metal borides, a subclass of refractory hard materials, are used in a variety of applications, including defense, the nuclear sector, and high-temperature industries.[1] Metal borides constitute a nascent category of improved electrocatalysts for the oxygen evolution reaction (OER), while also presenting a promising opportunity to customize their electrochemical characteristics for potential application in energy storage and conversion technologies.[2] The transition metals typically generate borides that are high in metal content. Metal-rich borides, collectively, exhibit inertness and possess elevated melting temperatures. A recent classification of ternary metal borides has been provided.[3] Numerous well-defined ternary metal borides have been identified and characterized, especially by Russian researchers. Only a limited number of studies on physical and chemical properties are known. Measurements have primarily been conducted on full and terminal solid solutions of binary metal borides, which may also provide insights into the behavior of ternary borides in some instances.[4] The crystal structures of the majority of ternary metal borides can be obtained from structural units that are assembled based on topochemical principles. A categorization of ternary metal borides can be established based on boron–boron aggregation, which is dependent on the boron to metal ratio.

Numerous studies on ternary metal borides have been conducted in recent years. In the course of various experimental investigations on transition metal borides, J. M. Leitnaker observed anomalous behavior in heated mixtures of Group IV metal diborides with tungsten and molybdenum.[5–7] Density functional theory simulations have been employed to discover stable layered crystal structure phases of Li–M–B, obtained from a recently reported binary metal-sandwich (MS) lithium monoboride superconductor. They demonstrate that the stability of MS lithium monoboride is enhanced when alloyed with electron-rich metal diborides.[8] Another study observed superconductivity at approximately 8 K in the metal-rich Li–Pd–B ternary system. This is the inaugural detection of superconductivity in metal-rich ternary borides comprising alkaline metals and palladium as a late transition metal.[9] A separate study

a Department of Physics, Dhaka University of Engineering and Technology (DUET), Gazipur, Gazipur-1707, Bangladesh

b Department of Physics, Bangabandhu Sheikh Mujibur Rahman Science and Technology University, Gopalganj-8100, Bangladesh.
E-mail: iamarpon07@gmail.com, arpon.phy@gstu.edu.bd

examined the auto-ignition sol–gel method for synthesizing ternary transition metal boride (TTMB) powders and analyzed their magnetic properties. The synthesized TTMB powders exhibited varying degrees of crystallinity and magnetic properties, contingent upon the boron-to-metal ratio and the subsequent incorporation of dysprosium into one of the samples.[10] This study employed semi-automated density functional theory (DFT) simulations to analyze transition metal diborides, focusing on their structural characteristics, phase stability, and mechanical properties. An intriguing aspect is the design of thin film materials, such as ternary or multilayer systems, enabling application-oriented coating development, aimed at concentrating experimental investigations on the most promising systems.[11] Transition metal borides exhibit hardness characteristics. The most resilient boride ($B_{12}C_3$) is utilized as a wear-resistant polycrystalline material, in armor tiles, and within the nuclear business, among other applications. The transition metal integrates into the crystal lattice of $B_{12}C_3$, forming new superhard ternary borides $B_{12-n}C_3$ with a hardness ranging from 50 to 77 GPa.[12]

The RE–[Ru, Rh]–B systems have been partially investigated by Matthias et al., and also RE[Ru, Rh]$_4$B$_4$ compounds exhibiting notable magnetic and superconducting properties have been documented.[13–15] Peter Rogl has synthesized novel ternary metal borides with the composition RET$_4$B$_4$ (where RE represents a rare earth metal and T denotes a transition metal) within the systems [La, Ce, Pr, Nd, Sm]–Os–B and [Y, La, Ce, Pr, Nd, Sm, Gd, Tb]–Ir–B. These compounds were seen to crystallize in the NdCo$_4$B$_4$-type structure.[16] Ku et al. report four new ternary boride systems with the CeCo$_3$B$_2$-type structure, characterized by the general formulae MRu$_3$B$_2$ (M = La, Ce, Pr, Nd, Sm, Gd, Tb, Dy, Ho, Er, Tm, Yb, Lu, Y, Th, or U), MRh$_3$B$_2$ (M = La, Ce, Pr, Nd, Sm, Eu, or Gd), MOs$_3$B$_2$ (M = Lu or U), and MIr$_3$B$_2$ (M = La, Th, or U).[17] The majority of members inside these systems were observed to exhibit either superconductivity or magnetic ordering. Superconductivity has been found in Ru$_3$B$_2$Th, where Th is a nonmagnetic element. The superconducting transition temperature ranges from 1.79 K to 1.6 K.[17]

The formula, lattice parameters, and powder intensities suggest a structural similarity between the new RERu$_3$B$_2$ family of compounds (space group P6/mmm, no. 191) and the structure type of CeCo$_3$B$_2$.[18] The crystal structure of Ru$_3$B$_2$U was determined using single-crystal four-circle diffractometer data and revealed a low-symmetry, fourfold superstructure ($a = 2a^*$, $c = 2c^*$) of the CeCo$_3$B$_2$ unit cell,[19] with a lower c/a ratio (~ 0.54) compared to CeCo$_3$B$_2$ (~ 0.55–0.57), indicating compressed axial stacking. This structural distortion in Ru$_3$B$_2$U arises from U's smaller ionic radius and stronger covalent interactions compared to that of Th or rare-earth elements in CeCo$_3$B$_2$. The magnetic properties and structural chemistry of the Ru-series compounds RERu$_3$B$_2$ were examined for an alternative space group, leading to a structural analogy with CeCo$_3$B$_2$, as determined from the single crystal analysis of ErRu$_3$B$_2$. A meticulous examination of the X-ray powder patterns of the uranium compounds U(Ru, Os)$_3$B$_2$, however, revealed a significantly different c/a ratio (0.542), prompting a comprehensive

exploration of their structural type in a previous study. The little divergence from the higher symmetry atomic configuration in the CeCo$_3$B$_2$ subcell (P6/mmm[20]) is evident from a preliminary revision of the Ru$_3$B$_2$U structure in space group P6$_3$/mmc, resulting in a reliability factor as low as $R \sim 10\%$.[19] While TiB$_2$ and ZrB$_2$ exhibit simple hexagonal AlB$_2$-type structures with planar B layers, Ru$_3$B$_2$X incorporates actinide atoms (Th/U) in prismatic sites, introducing additional bonding complexity and reducing direct B–B bonding (B–B distances > 3 Å vs. ~ 1.8 Å in TiB$_2$). The magnetic susceptibility of Y, Lu, Th, and U compounds was determined to be mostly temperature-independent, hence categorizing [Y, Lu, U, Th]Ru$_3$B$_2$ and UOs$_3$B$_2$ as Pauli paramagnets. The majority of the remaining RERu$_3$B$_2$ borides displayed typical paramagnetic behavior and closely followed the Curie–Weiss law over the significant temperature range of 300–1100 K.[18]

Our study focuses on Ru$_3$B$_2$X (X = Th, U) due to their unique structural stability with a unique combination of hexagonal symmetry, mechanical properties, and potential applications in high-temperature environments and IR shielding materials. Unlike other RERu$_3$B$_2$ compounds, Ru$_3$B$_2$X compounds exhibit a combination of strong covalent bonding and moderate ductility, making them particularly interesting for technological applications. Ru$_3$B$_2$Th and Ru$_3$B$_2$U are understudied compared to other RERu$_3$B$_2$ compounds. Additionally, experimental studies on these compounds are limited, making theoretical insights especially valuable.

2. Computational method

In this study, we employed the Cambridge serial total energy package (CASTEP) software to examine the characteristics of Ru$_3$B$_2$X (X = Th, U) utilizing density-functional theory (DFT).[21,22] In order to calculate the exchange–correlation energy, we utilize the generalized gradient approximation (GGA) in conjunction with the Perdew–Burke–Ernzerhof (PBE) exchange–correlation functional.[23] In the realm of electron–ion interactions, ultrasoft pseudopotentials are the defining characteristics.[24] When it comes to Ru$_3$B$_2$X (X = Th, U), the electron wave function is represented by plane waves that have a cut-off energy of 500 eV. The Monkhorst–Pack technique[25] is in charge of producing a consistent grid of k-points along the three axes in reciprocal space in order to sample the Brillouin zone. Within this grid, $5 \times 5 \times 8$ special k-points were chosen for the purpose of optimizing the geometry of Ru$_3$B$_2$X. In order to determine the equilibrium crystal structure of Ru$_3$B$_2$X (X = Th, U), the Broyden–Fletcher–Goldfarb–Shanno (BFGS) minimization algorithm[26] was utilized. The following is a list of the criteria that were defined for the optimization of geometry. It was determined that the total energy of the atom was 1.0×10^{-6} eV, the maximum force was 0.03 eV Å^{-1}, the greatest stress was 0.05 GPa, and the maximum atomic displacement was 0.001 Å.

The bulk modulus, electronics characteristics, and elastic constants C_{ij} were all computed directly by using the CASTEP code. The polycrystalline elastic constants are inferred from the

computed C_{ij} using the Voigt–Reuss–Hill (VRH) approximation approach.[27] The Kleinman parameter (ζ), which evaluates a compound's resistance to stresses like stretching and bending, is another helpful metric. The thermal properties of crystalline materials are crucial for the direct explanation of many solid-state phenomena.[28] Debye temperatures, specific heats, melting temperature, thermal conductivity, and thermal expansion coefficient have all been evaluated for our compounds.

The energy band structure of materials is directly proportional to the frequency-varying complex dielectric function, $\varepsilon(\omega)$. Drude damping[29] is required for the study of optical constants in metallic materials. The optical constants of Ru_3B_2X were calculated using the CASTEP technique with a screened plasma energy of 3 eV and a Dude damping of 0.5 eV. We were able to correct the imaginary part of the dielectric function by using the momentum matrix components that fall between the wave functions of the occupied and unoccupied states. The imaginary component $\varepsilon_2(\omega)$ of the dielectric function in this study is as follows:

$$\varepsilon_2(\omega) = \left(\frac{4\pi^2 e^2}{m^2\omega^2}\right) \sum_{ij} \int \langle i|M_d|j\rangle^2 f_i(1-f_i)\delta(E_f - E_i - \omega)\mathrm{d}^3k$$

(1)

Here, i represents the initial state and j represents the final state. Also, M_d denotes the dipole matrix, f_i denotes the Fermi distribution function, and E_i represents the energy of the electron in the i-th state. We can obtain the real portion of the dielectric function with the help of the Kramers–Kronig relation and it can be represented as

$$\varepsilon_1(\omega) = 1 + \frac{2}{\pi}P\int_0^\infty \frac{\omega'\varepsilon_2(\omega')\mathrm{d}\omega'}{(\omega'^2 - \omega^2)}$$

(2)

where P represents the principal value of the integral. This study presents and analyzes the reflectivity, optical conductivity, refractive index, and extinction coefficient.[30] The Kramers–Kronig relation serves as a valuable tool in assessing the complex dielectric constant, which in turn enables the calculation of optical characteristics. This relationship plays a crucial

role in solid-state optics by providing insights into a material's behavior and facilitating the determination of various optical parameters.

Ab initio molecular dynamics (AIMD) simulation was performed using the Vienna *ab initio* simulation package (VASP).[31,32] The simulations were performed for 1000 femtoseconds. VASPKIT[33] was used to analyze the output. To check the stability energetically, single-atom energies were computed, using the same pseudopotentials and functional (GGA-PBE) as for the bulk system.

3. Results and discussion

3.1 Structural properties

The crystal structure of Ru_3B_2X (X = Th, U) is hexagonal with space group $P6/mmm$ (no. 191). The optimized unit cell is depicted in Fig. 1(a). We perform our calculation at zero external pressure and the results of the first principles calculations of structural properties are presented in Table 1. A high degree of reliability of the computational methods used is indicated by the good agreement between our estimated values of lattice constants and volume and the experimental data.[17–19]

3.1.1 Structural building blocks and atomic arrangement. The structure of Ru_3B_2X (X = Th, U) can be visualized as comprising three distinct structural building blocks, as shown in Fig. 1(b).

X-Centered hexagonal prisms: the X atoms (Th or U) occupy the 1a Wyckoff position (0, 0, 0) and are coordinated by 12 Ru atoms forming a hexagonal prism. These prisms are arranged in a hexagonal pattern in the ab-plane and share faces along the c-axis.

B-Centered trigonal prisms: the B atoms occupy the 2c Wyckoff position (1/3, 2/3, 0) and are coordinated by 6 Ru atoms forming a trigonal prism. These B-centered trigonal prisms share edges with neighboring prisms, forming a continuous network in the ab-plane.

Ru coordination polyhedra: the Ru atoms, located at the 3g Wyckoff position (1/2, 0, 1/2), exhibit a complex coordination
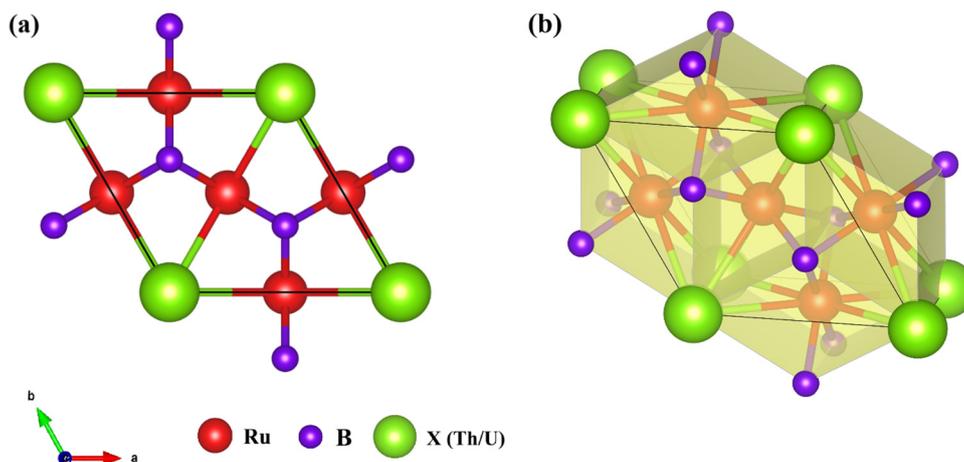

Fig. 1 (a) Optimized crystal structure of the Ru_3B_2X (X = Th, U) unit cell and (b) structural building blocks of Ru_3B_2X (with polyhedra).

Table 1 Calculated lattice parameters $a = b$ and c (both in Å), equilibrium volume V (Å^3), and formation enthalpy ΔH_f (eV per atom) of Ru$_3$B$_2$U and Ru$_3$B$_2$Th at 0 GPa

Compound	a	c	c/a	V	ΔH_f	Ref.
Ru$_3$B$_2$U	5.508	2.976	0.54	78.196	−9.12	This work
	5.476	2.960	0.54	76.869	—	17[Expt]
	5.475	2.967	0.54	77.022	—	18[Expt]
	5.477	2.968	0.54	77.104	—	19[Expt]
Ru$_3$B$_2$Th	5.571	3.068	0.55	82.469	−8.84	This work
	5.526	3.070	0.55	81.188	—	17[Expt]
	5.528	3.070	0.55	81.200	—	18[Expt]

environment. Each Ru atom is bonded to 4 B atoms and 4 X atoms, forming a distorted square antiprism. The Ru atoms serve as the connective tissue between the X and B layers.

3.1.2 Coordination environments. X (Th/U) coordination: the actinide atoms (Th or U) are surrounded by 12 Ru atoms in a hexagonal prismatic arrangement. The X–Ru bond lengths are calculated to be 3.02 Å for Ru$_3$B$_2$Th and 2.94 Å for Ru$_3$B$_2$U, indicating a more compact coordination environment in the uranium compound. This coordination environment is characteristic of metal-rich borides and contributes to the stability of the structure.

B coordination: each B atom is surrounded by 6 Ru atoms forming a trigonal prism. The B–Ru bond lengths are 2.21 Å for Ru$_3$B$_2$Th and 2.18 Å for Ru$_3$B$_2$U. Notably, the B atoms form a planar honeycomb-like network in the *ab*-plane, with no direct B–B bonds observed (B–B distances exceed 3 Å), distinguishing this structure from boron-rich borides.

Ru coordination: the Ru atoms exhibit a mixed coordination environment with 4 B neighbors and 4 X neighbors. The Ru–B bonds (2.18–2.21 Å) are significantly shorter than the Ru–X bonds (2.94–3.02 Å), reflecting the stronger covalent character of the Ru–B interaction compared to the more metallic Ru–X bonding.

3.1.3 Energetic stability. In order to verify the structural stability of the two compounds, the formation enthalpy of each compound can be computed using the existing relationships,

where the formation enthalpies of the compounds were determined by deducting the energy of each of the constituent elements from the total energy. The negative enthalpy value of Ru$_3$B$_2$U and Ru$_3$B$_2$Th indicates that both compounds are thermally stable. Moreover, the negative enthalpy signifies that the lattice generation is thermodynamically advantageous, implying that the process will naturally take place assuming normal conditions.

$$\Delta H_f(Ru_3B_2X) = E_{total}(Ru_3B_2X) - 3E(Ru) - 2E(B) - E(X) \quad (3)$$

To check the structural stability more precisely, we have conducted *ab initio* molecular dynamics (AIMD) simulation for 1000 femtoseconds (fs). From Fig. 2(a), it can be seen that Ru$_3$B$_2$Th stabilizes at a lower average temperature. Ru$_3$B$_2$U maintains a higher temperature on average, with smaller amplitude fluctuations around that higher value. On the other hand, Fig. 2(b) indicates that Ru$_3$B$_2$Th starts at a higher total energy (around ∼355 eV) and relaxes over the first ∼200 fs to about ∼375 eV, after which it fluctuates only slightly. Ru$_3$B$_2$U (black curve) remains near ∼−58 eV the entire time with small fluctuations, suggesting that it was already close to an equilibrium state (or at least a shallow minimum) under the chosen simulation conditions.

So, it can be concluded that Ru$_3$B$_2$Th relaxes to a deeper potential-energy minimum and remains there with a lower thermal energy. In contrast, Ru$_3$B$_2$U appears stable in its own shallower energy minimum at a higher temperature.

3.2 Mechanical properties

The selection of materials capable of withstanding particular loads and stresses, by engineers and designers, is dependent on mechanical characteristics like tensile strength, elasticity, ductility, and toughness. Moreover, comprehensive knowledge of such properties facilitates the optimization of several heat treatment procedures. In the subsequent sub-sections, we will provide the computed mechanical properties that characterize the parameters of Ru$_3$B$_2$X (X = Th, U) compounds.
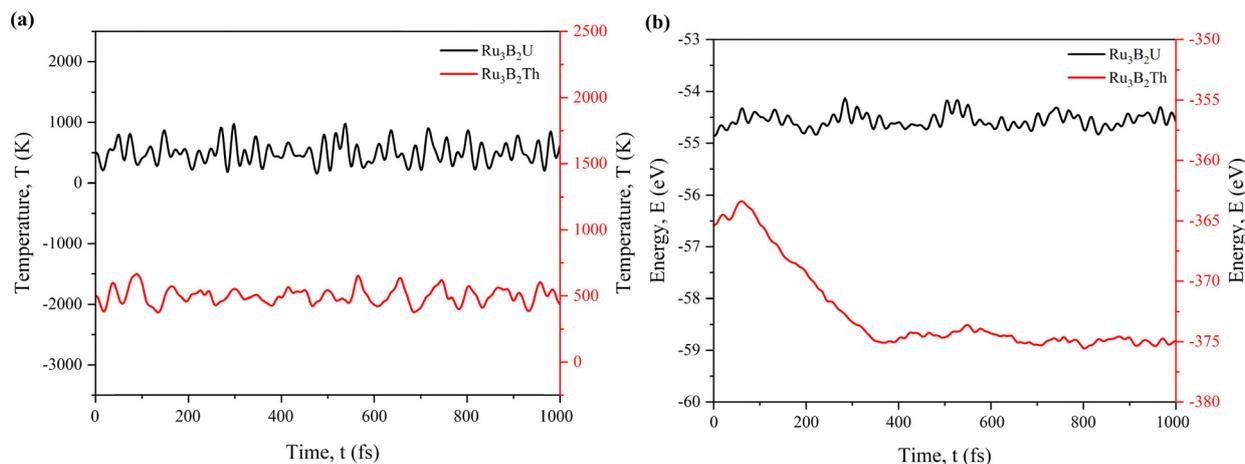
Fig. 2 Change of (a) temperature and (b) energy with time for Ru$_3$B$_2$U and Ru$_3$B$_2$Th.

3.2.1 The stiffness constant: mechanical stability. Establishing the elastic constants of a material is essential for comprehending its mechanical properties, particularly its reaction to stress and strain. The determination of stiffness constants is also associated with the response of the crystal to thermal stress. Initially, we compute the elastic constants (C_{ij}) of Ru_3B_2X (X = Th, U) using the stress–strain method implemented in the CASTEP code. The obtained elastic constants (C_{ij}) are presented in Table 2. The hexagonal crystalline structure of Ru_3B_2X (X = Th, U) is generally recognized to result in six stiffness constants (C_{11}, C_{12}, C_{13}, C_{33}, C_{44}, and C_{66}). The first five constants are independent, while the last one (C_{66}) can be derived from constants that characterize the elastic reaction to normal stresses specifically along the principal crystallographic axes namely C_{11} and C_{12}. Constants C_{44} and C_{66} characterize the ability of the material to withstand shear stress on planes that are perpendicular to the main axis and shear deformations in various directions inside the hexagonal plane respectively, while C_{13} is closely related to the Poisson effect in hexagonal crystals. A hexagonal system must meet the following inequality criteria for mechanical stability, as per Born–Huang assumptions:[34,35]

$$C_{11} > 0, C_{33} > 0, \quad C_{44} > 0, \quad C_{11} - |C_{12}| > 0,$$
$$C_{33}(C_{11} + C_{12}) - 2C_{13}^2 > 0 \qquad (4)$$

The computed values of C_{ij} shown in Table 2 correspond to the aforementioned relationships and indicate that the Ru_3B_2X (X = Th, U) compounds we investigated exhibit mechanical stability. The superiority of C_{11} over C_{33} indicates more robust atomic interactions along the a-axis compared to the c-axis. The strong adhesion along the a-axis suggests increased resistance to distortion caused by the a-axis. The observation that C_{11} and C_{33} exhibit higher values compared to C_{44} implies that shear deformation is more readily accommodated than axial strain. The shear constant ($C' = (C_{11} - C_{12})/2$) is a parameter that quantifies the stiffness of the crystal and also determines the dynamical stability of a crystalline material. The positive value of C', as listed in Table 2, numerically equal to C_{66} for our examined crystal structure, indicates that Ru_3B_2X (X = Th, U) is dynamically stable.

3.2.2 Elastic moduli, and brittleness/ductility indicator. To characterize Ru_3B_2X (X = Th, U), several bulk elastic parameters, including Young's modulus (Y), bulk modulus (B), and shear modulus (G), are determined using our computed elastic constants. A greater magnitude of these parameters signifies the superior capacity of the materials to withstand tensile, uniform compressive or volume, and shear deformations, respectively. The acoustic mode is accountable for thermal transfer just because of its substantial group velocity which is further influenced by Young's modulus and the mass density $\left(v_s = \sqrt{Y/\rho}\right)$. The elastic moduli are linked with thermal conductivity (K_L) as $K_L \tilde{\sqrt{Y}}$.[36] Moreover, an essential factor in the design of materials for acoustic applications is the impact of the bulk modulus (B) on the speed of sound in a material. We calculated these parameters using the Voigt–Reuss–Hill (VRH) approximation,[37–40] and our findings are tabulated in Table 3.

The higher Y values imply that Ru_3B_2X (X = Th, U) are stiffer compounds and the stiffness follows the order Ru_3B_2U > Ru_3B_2Th. Furthermore, the thermal shock resistance (R) is inversely related to Y, making it a crucial determinant for choosing compounds as thermal barrier coating (TBC) materials.[41,42] The Y value suggests that the compounds Ru_3B_2X (X = Th, U) have the potential to be used as TBC materials,[42] and Ru_3B_2Th is a more effective TBC material than Ru_3B_2U. The comparison of the thermal coating ability of our compounds with $Y_3Al_5O_{12}$ ($Y = 290$ GPa)[42] gives rise to the order Ru_3B_2Th > $Y_3Al_5O_{12}$ > Ru_3B_2U.

The brittleness and ductility of a material can be characterized by two parameters, namely Poisson's (ν) and Pugh's ratio (B/G), which are derived from elastic moduli. Table 4 lists the values of these parameters. The criteria $\nu > 0.26$ and $B/G > 1.75$ determine the ductility of a material; otherwise, it is brittle.[43,44] Consequently, the material Ru_3B_2X (X = Th, U) is predicted to be ductile. It is a rare feature in hard borides. In addition, it is observed that Ru_3B_2Th exhibits more ductility than Ru_3B_2U. Besides this, Poisson's ratio can also indicate the characteristics of the bonding of a molecule. Given that Ru_3B_2X (X = Th, U) meets the limiting condition $0.25 \leq \nu \leq 0.50$, the

Table 2 Calculated elastic constants C_{ij} (GPa) and shear constant C' (GPa)

Compound	C_{11}	C_{12}	C_{13}	C_{33}	C_{44}	C_{66}	C'
Ru_3B_2U	464.86	166.56	147.35	451.97	107.88	149.15	149.15
Ru_3B_2Th	339.61	134.74	136.84	329.96	82.40	102.44	102.43

Table 4 Poisson's ratio (ν), Pugh's ratio (B/G), Cauchy pressure (C'' in GPa), Kleinman parameter (ξ), machinability index (μ_M), hardness values (H_{macro} and H_{micro} in GPa), and fracture toughness (K_{IC} in MPa m$^{0.5}$)

Compound	ν	B/G	C''	ξ	μ_M	H_{macro}	H_{micro}	K_{IC}
Ru_3B_2U	0.279	1.93	58.68	0.501	2.372	13.136	19.489	2.824
Ru_3B_2Th	0.301	2.18	52.35	0.536	2.462	8.388	12.333	2.126

Table 3 Young's modulus Y (GPa), bulk modulus B (GPa), and shear modulus G (GPa). The subscripts V, R, and H denote Voigt, Reuss, and Hill approximations, respectively

Compound	Y			B			G		
	Y_V	Y_R	Y_H	B_V	B_R	B_H	G_V	G_R	G_H
Ru_3B_2U	343.03	334.72	338.88	256.02	255.78	255.90	134.34	130.56	132.45
Ru_3B_2Th	243.14	241.01	242.08	202.89	202.87	202.88	93.50	92.56	93.03

influence of central force interaction and ionic contribution is crucial in both compounds.[45,46] Another significant stress property of materials that quantifies the ductility or brittleness of components is the Cauchy pressure ($C'' = C_{12} - C_{44}$),[47] which is presented in Table 4. Ductility and the presence of an ionic bond in a compound are probable when the Cauchy pressure is positive, whereas negative values indicate brittleness.[48] The positive nature of C'' suggests the ductility and predominance of ionic bonding in Ru_3B_2X (X = Th, U).

3.2.3 Internal strain parameter, machinability criteria, hardness, and fracture toughness. The internal strain parameter, commonly known as the Kleinman parameter (ξ), is helpful for determining the relative positioning of cation and anion sub-lattices in response to volume-preserving strain distortions.[49] One may estimate the dimensionless Kleinman parameter of a chemical using the following relation:[46]

$$\xi = \frac{C_{11} + 8C_{12}}{7C_{11} + 2C_{12}} \tag{5}$$

The values of ξ of Ru_3B_2X (X = Th, U) are listed in Table 4 and are typically within the range of zero to one ($0 \leq \xi \leq 1$). These minimum and maximum limits represent the minimal impact of bond bending and the minimal impact of bond stretching/contraction, respectively, in resisting external force. The computed value of ξ for Ru_3B_2X (X = Th, U) demonstrates that the mechanical strength of Ru_3B_2X (X = Th, U) is substantially influenced by both bond bending and bond stretching/contraction contributions.

The machinability index, μ_M, of a material is a reliable measure of its effectiveness. It is an essential determinant of the elastic properties or characteristics of the working materials.[50] Moreover, it is beneficial for quantifying the plasticity[51,52] and lubricating characteristics of a substance. The assessment of μ_M is made using the equation B/C_{44}, where B is the bulk modulus. Table 4 reports the μ_M of Ru_3B_2X (X = Th, U), and based on our findings, though Ru_3B_2Th exhibits great machinability compared to Ru_3B_2U, both compounds are equally appropriate for use in manufactured machines.

The hardness of Ru_3B_2X (X = Th, U) compounds was determined by the application of the following formulae:

$$H_{macro} = 2\left[\left(\frac{G}{B}\right)^2 G\right]^{0.585} - 3 \tag{6}$$

$$H_{micro} = \frac{(1 - 2\nu)E}{6(1 + \nu)} \tag{7}$$

The relationship between hardness and crystalline elastic modulus is highly interdependent and directly impacts their resistance to notching forces. From Table 4, Ru_3B_2U is anticipated to exhibit higher hardness between the compounds considering the stated value (H_{macro} = 13.136 GPa), whereas Ru_3B_2Th has a low hardness value (H_{macro} = 8.388 GPa). Overall, Ru_3B_2X shows moderate hardness, lower than superhard borides like $B_{12}C_3$ ($\sim$50–77 GPa) but higher than ductile borides such as Fe_2B ($\sim$8 GPa). The capacity of a material to withstand

the spread of cracks and fractures under external forces is represented by fracture toughness K_{IC}, which can be calculated using the formula published by Niu *et al.*:[53]

$$K_{IC} = V_0^{1/6} G(B/G)^{0.5} \tag{8}$$

The constant V_0 represents the final volume per atom of the unit cell, and the obtained value of K_{IC} of Ru_3B_2X (X = Th, U) is shown in Table 4. The superior fracture toughness of Ru_3B_2U compared to Ru_3B_2Th allows it to endure greater applied pressures without undergoing crack propagation, rendering it more appropriate for load-bearing structures. Moreover, K_{IC} is related to the brittleness index (M_B) and hardness (H_V) by the equation $M_V = H_V/K_{IC}$.

3.2.4 The elastic anisotropy. A wide range of physical processes, including plastic deformation in solids and the creation of micro-scale fracture, are influenced by mechanical anisotropy in solid materials.[54] We can elucidate the direction-dependent mechanical behavior by considering these parameters. Anisotropy factors A_1, A_2, and A_3, also referred to as shear anisotropy factors, are related to the shear planes {100}, {010}, and {001} between directions 011 and 010, 101 and 001, and 110 and 100, respectively. Deviation of the values of A_i (i = 1, 2, 3) from unity indicates the anisotropic character of the compounds being studied,[55,56] and can be obtained by the following equations:

$$A_1 = \frac{4C_{44}}{C_{11} + C_{33} - 2C_{13}} \tag{9}$$

$$A_2 = \frac{4C_{55}}{C_{22} + C_{33} - 2C_{23}} \tag{10}$$

and

$$A_3 = \frac{4C_{66}}{C_{11} + C_{22} - 2C_{12}} \tag{11}$$

The shear anisotropic factors for Ru_3B_2X (X = Th, U) have been computed and are presented in Table 5. The findings indicate that Ru_3B_2U exhibits a higher degree of anisotropy, whereas Ru_3B_2Th has a lower amount of anisotropy. The concept of the universal anisotropy index (A^U) was introduced by Ranganathan and Ostoja-Starzewski,[57] which offers a unidimensional measure of anisotropy, independent of the crystal symmetry. This also encompasses the impact of the bulk on the anisotropy of a solid and is measured solely as zero or positive. A value of A^U equal to zero indicates that the crystal is isotropic, while any value other than zero suggests the existence and degree of anisotropy. The value of A^{eq}, the equivalent Zener anisotropy measure, for an isotropic crystalline material is 1. The conventional formulae for estimating the universal anisotropy index A^U, equivalent Zener anisotropy measure A^{eq}, anisotropy in compressibility A^B, and anisotropy in shear A^G (or A^C) for a material with any symmetry are as follows:[58–60]

$$A^U = 5\frac{G_V}{G_R} + \frac{B_V}{B_R} - 6 \geq 0 \tag{12}$$

Table 5 Calculated shear anisotropic factors (A_1, A_2, and A_3), universal anisotropy index (A^U), equivalent Zener anisotropy measure (A^{eq}), anisotropy in shear (A^G or A^C), anisotropy in compressibility (A^B), linear compressibility (β_a and β_c in TPa^{-1}) and linear compressibility ratio (β_a/β_c) for Ru$_3$B$_2$X (X = Th, U)

		Compound	
Anisotropy factors		Ru$_3$B$_2$U	Ru$_3$B$_2$Th
Shear anisotropy factors	A_1	0.694	0.833
	A_2	0.694	0.833
	A_3	1.000	1.000
Universal and Zener anisotropy	A^U	0.146	0.051
	A^{eq}	1.091	1.032
Shear and compressibility anisotropy	A^G	0.014	0.005
	A^B	0.00047	0.00005
Linear compressibility	β_a	0.007	0.004
	β_c	0.008	0.005
	β_a/β_c	0.875	0.800

$$A^{eq} = \left(1 + \frac{5}{12}A^U\right) + \sqrt{\left(1 + \frac{5}{12}A^U\right)^2 - 1} \qquad (13)$$

$$A^B = \frac{B_V - B_R}{B_V + B_R} \qquad (14)$$

$$A^G = \frac{G_V - G_R}{2G_H} \qquad (15)$$

Table 5 lists all the above mentioned anisotropic factors. The value of A^U of Ru$_3$B$_2$X (X = Th, U) signifies that both compounds display anisotropy, but the anisotropy of Ru$_3$B$_2$Th is rather minimal (A^U = 0.051). The predicted value of A^{eq} for Ru$_3$B$_2$X (X = Th, U) additionally suggests that the compounds are anisotropic. Moreover, the positive departure of A^B and A^G from zero indicates the level of anisotropy. Our findings indicate that Ru$_3$B$_2$U consistently displays a higher degree of anisotropy compared to Ru$_3$B$_2$Th. In Ru$_3$B$_2$X (X = Th, U), the difference between the values of A^G and A^B (Table 5) suggests that the anisotropy in shear is greater than the anisotropy in compressibility.

The linear compressibility of a hexagonal crystal along the a and c axes (β_a and β_c) can be determined using the following equations:[61]

$$\beta_a = \frac{C_{33} - C_{13}}{D} \qquad (16)$$

$$\beta_c = \frac{C_{11} + C_{12} - 2C_{13}}{D} \qquad (17)$$

where $D = (C_{11} + C_{12})C_{33} - 2(C_{13})^2$. The computed values are present in Table 5, and the results suggest that the compressibility along the a and c axes has anisotropic characteristics, while the anisotropic bulk modulus clearly demonstrates directional anisotropy in Ru$_3$B$_2$X (X = Th, U).

With the aid of the ELATE program,[62] the directional dependence of Young's modulus (Y), linear compressibility (β), Shear modulus (G), and Poisson ratio (ν) of the crystal Ru$_3$B$_2$X (X = Th, U) is investigated using both 2D and 3D graphical projection. The necessary elastic stiffness matrices for this work are calculated using the CASTEP model. Uniform circular two-dimensional and spherical three-dimensional graphical representations are physical manifestations of the isotropic properties of crystals.

The level of anisotropy increases proportionally with the extent of departure from these ideal forms. Fig. 3 and 4 illustrate the 2D projection of the compound on the xy-, xz-, and yz-planes, as well as the 3D analysis of Y, β, G, and ν, for Ru$_3$B$_2$Th and Ru$_3$B$_2$U respectively. The curves in green and blue correspond to the minimum and maximum values for the parameters, respectively. Evidently, all four parameters exhibit isotropy in the xy-plane and anisotropy in other planes. Furthermore, the figures clearly show that the anisotropy in linear compressibility (β) is almost negligible for both compounds.

3.3 Electronic properties

Determining the electronic characteristics of materials is essential for developing technology and innovation in a variety of sectors. The design and functionality of electronic devices are influenced by electronic qualities including band structure, electronic charge density, density of states, bond population analysis, and Fermi surface topology, which have a direct impact on how materials react to electric fields and currents. In essence, investigating electronic characteristics results in the discovery of novel materials, expanding our knowledge of the physics of condensed matter and materials science.

3.3.1 Electronic band structure. The optimized lattice has been used to study the electronic band structure (EBS) in order to comprehend the electronic behavior of the Ru$_3$B$_2$X (X = Th, U) compounds. The band structures of Ru$_3$B$_2$X (X = Th, U) were calculated along the high-symmetry direction (Γ–A–H–K–Γ–M–L–H) of the first Brillouin zone to investigate its electronic properties. The obtained band structures at 0 GPa are displayed in Fig. 5. The horizontal red dashed line in the figure represents the Fermi level (E_F).

An important contribution of electronic states to electrical conductivity is indicated by the band dispersion close to the Fermi level. As evident from the band structures, several electronic bands marked by green lines cross the Fermi level, confirming the metallic character of Ru$_3$B$_2$X (X = Th, U). In contrast to Ru$_3$B$_2$U, Ru$_3$B$_2$Th shows more metallic behavior because its conductivity is enhanced by a higher density of states at E_F, which is likely caused by the Fermi energy intersecting with more bands. Additionally seen is the topological nontrivial electronic band structure, which consists of slightly overlapping bands at specific places (K, Γ, and M points) in the Brillouin zone with several Dirac points. In some areas of the $E(k)$ figure, nearly linear dispersive bands are visible. For instance, the quasi-linear electronic dispersions close to the Fermi level refer to a relatively high degree of mobility, which
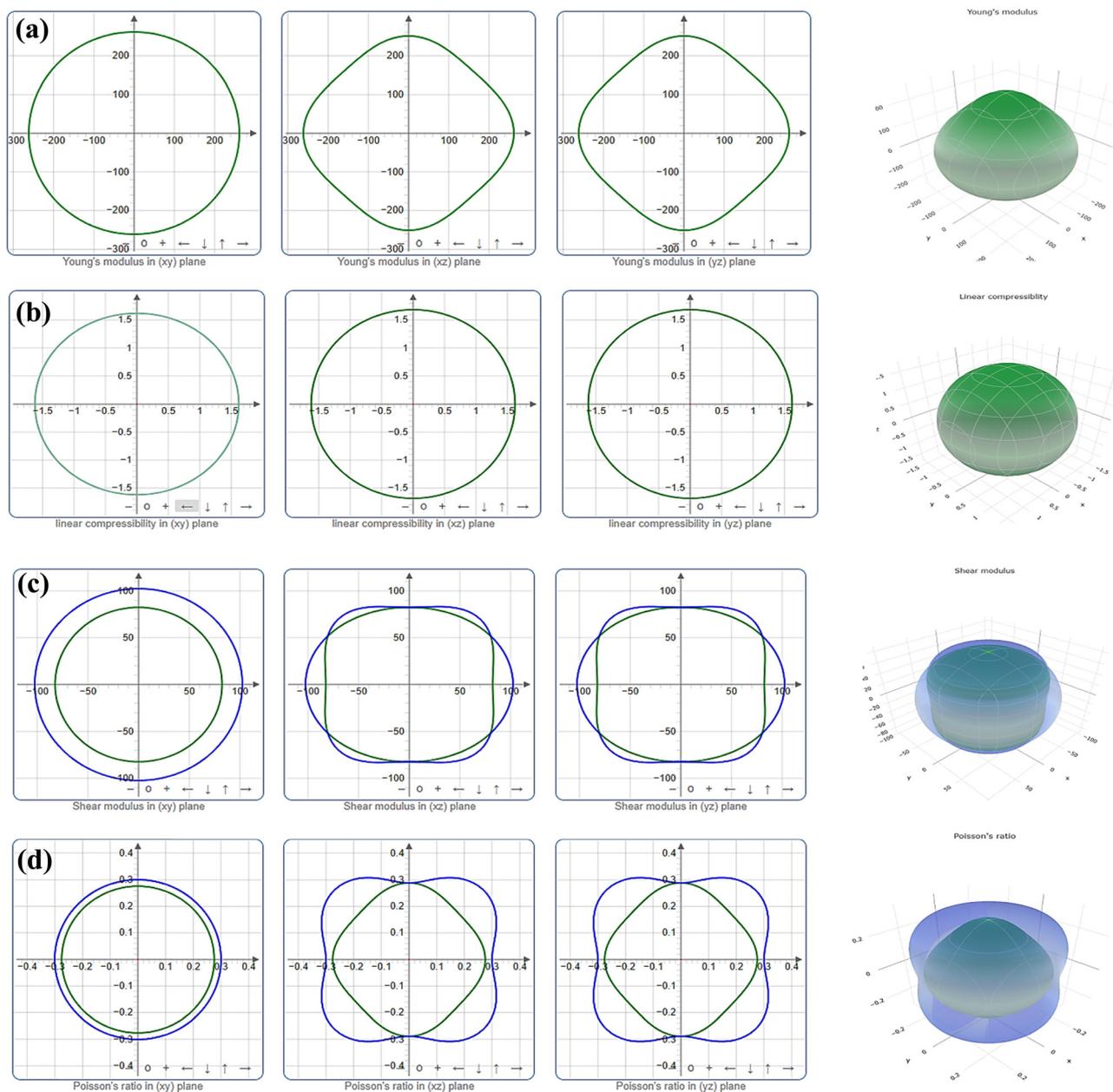
Fig. 3 Directional dependence of (a) Young's modulus (Y), (b) linear compressibility (β), (c) shear modulus (G), and (d) Poisson's ratio (ν) of Ru_3B_2Th.

results from the effective masses of the charge carriers and the corresponding wave vectors being substantially tiny.

3.3.2 Electronic energy density of states (DOS). For improved comprehension of the bonding nature between atoms and the contribution of various atomic orbitals to different types of conductivity and other electronic transport properties, it is beneficial to study the total and partial electronic density of states of materials. Moreover, the electronic contribution to spin paramagnetic susceptibility and metal heat capacity is closely correlated with the electronic density of states at the Fermi level.[63] The calculated total and partial density of states (TDOS and PDOS, respectively) of Ru_3B_2X

(X = Th, U) as a function of energy are displayed in Fig. 6, where the vertical dashed line indicates E_F.

The presence of metallic electrical conductivity in Ru_3B_2X (X = Th, U) is implied by the non-zero value of TDOS at the Fermi level. The computed values of TDOS at the Fermi level for Ru_3B_2U and Ru_3B_2Th are 6.13 and 4.76 per eV per unit cell, respectively, from Fig. 6(a) and (b), suggesting that Ru_3B_2U exhibits better electrical conductivity than Ru_3B_2Th. In contrast, Ru_3B_2Th has greater stability than Ru_3B_2U. Although Ru_3B_2Th has more conduction channels intersecting the Fermi level (Section 3.3.1), Ru_3B_2U has a higher density of states, both of which contribute differently to conductivity. So, it can be
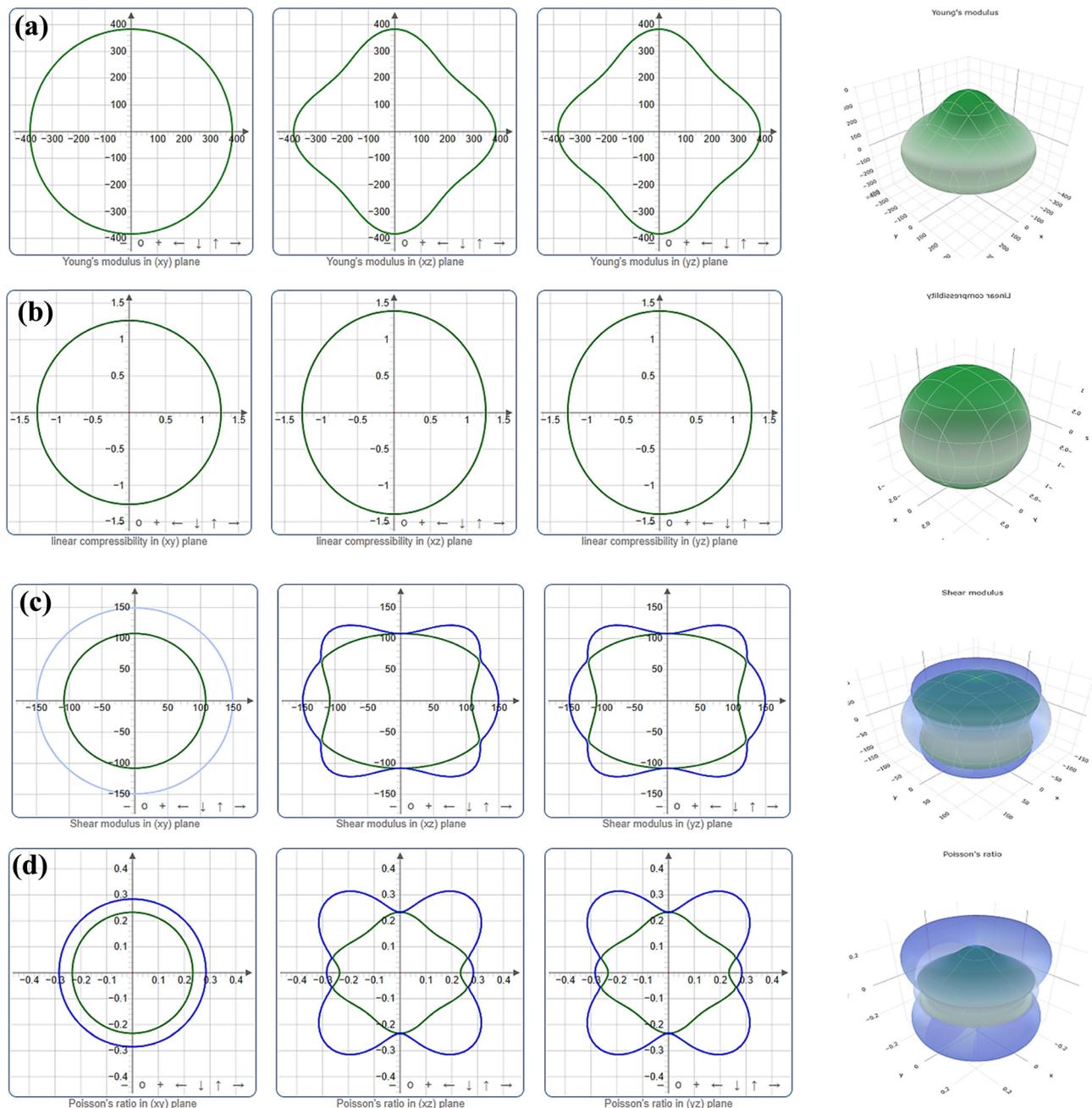
Fig. 4 Directional dependence of (a) Young's modulus (Y), (b) linear compressibility (β), (c) shear modulus (G), and (d) Poisson's ratio (ν) of Ru_3B_2U.

concluded that both compounds have good electrical conductivity. Ru-4d orbitals are the source of most of the electronic states close to the Fermi level; however B-2p states play a role at lower energy levels. Additionally, the U-5f orbital clearly plays a major role in the TDOS of Ru_3B_2U. A high density of accessible states for conduction is shown by the steep peaks in the TDOS at 0 GPa in Fig. 6, which are located just below the Fermi level. The TDOS of Ru_3B_2U has significant peaks around E_F at -1.37 and 1.02 eV. The hybridization of Ru-4d and U-5f orbitals results in the emergence of these bonding/anti-bonding peaks. The anti-bonding peaks of Ru_3B_2Th near E_F are quite dissimilar

to those in Ru_3B_2U. Furthermore, the presence of a deep valley in the TDOS plots of Ru_3B_2X (X = Th, U) near E_F is known as a pseudogap or quasi-gap, which is associated with the electronic stability of a material and separates the bonding states from the anti-bonding states.[64] Additionally, as the pseudogap position is extremely close to E_F, covalent bonding is present in the crystals, indicating that the materials are very resilient and have excellent mechanical properties.

An essential factor in identifying electronic correlations in a system is the electron–electron interaction (EEI) caused by the Coulomb force, commonly referred to as the repulsive Coulomb
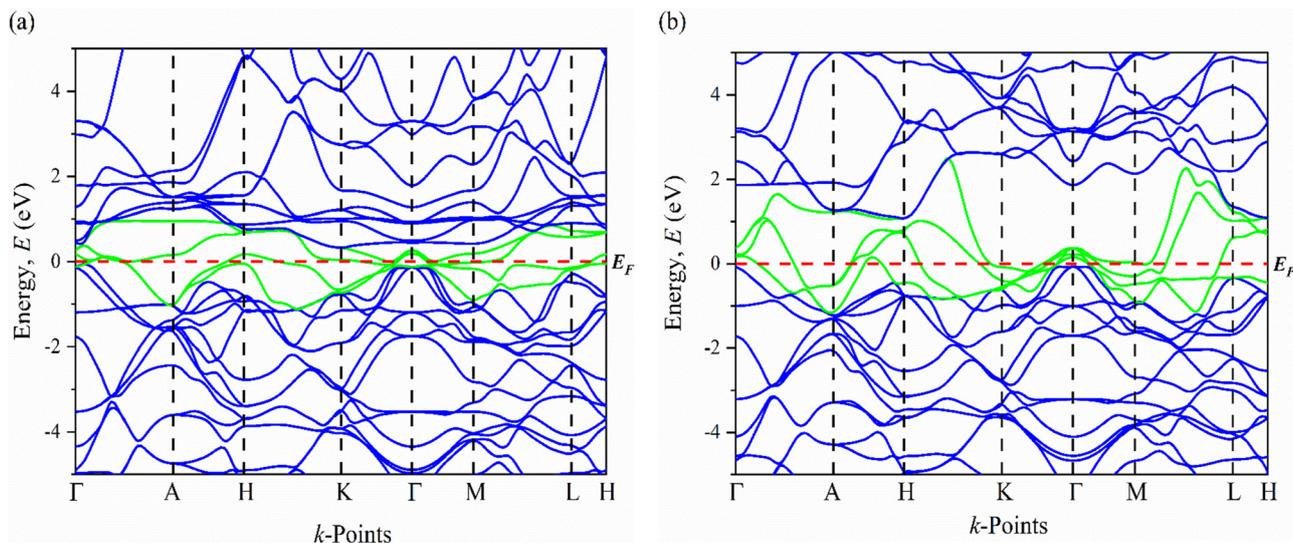
Fig. 5 The electronic band structures of (a) Ru_3B_2U and (b) Ru_3B_2Th along the high symmetry directions.

pseudopotential. It gives us a sense of how strong the direct Coulomb repulsion between electrons is and can be calculated using the following formula:[65]

$$\mu^* = \frac{0.26 N(E_F)}{1 + N(E_F)} \tag{18}$$

In the ground state, the predicted Coulomb pseudopotential values for Ru_3B_2U and Ru_3B_2Th are 0.223 and 0.215, which are relatively high and suggest significant electronic correlations.

3.3.3 Fermi surface topology. The electrical characteristics, superconducting potential,[66] and charge transport behavior of a material are significantly influenced by its Fermi surface topology. Fig. 7 illustrates the Fermi surfaces of Ru_3B_2X (X = Th, U) compounds produced using their corresponding electronic band structures. Cylindrical sheets extending along the vertical direction could reflect quasi-2D bands. The Fermi of Ru_3B_2U shows a simpler topology with fewer, isolated ellipsoidal pockets close to high-symmetry points. Because of its more isotropic nature, this Fermi surface indicates less spatial anisotropy, which is associated with lower conductivity, as well as lower carrier density and semi-metallic properties.

Conversely, in the case of Ru_3B_2Th, smaller Fermi surface pockets, perhaps at various energy bands, are indicated by the gray lobes spreading outward, while the larger, linked blue region shows massive electron or hole pockets centered around the Γ point. This complexity in the Fermi surface indicates a high carrier density, which implies metallicity and the possibility of charge density wave (CDW) production or superconductivity. Compared to the Fermi surface of Ru_3B_2U, which suggests conduction channels that are limited, the Fermi surface of Ru_3B_2Th supports better conductivity and enhanced electronic interactions, demonstrating the impact of band structure complexity on material performance.

3.3.4 Electronic charge density distribution. The bonding property and charge transmission among the atoms of Ru_3B_2X (X = Th, U) were demonstrated by projecting the electronic charge density distribution around the atoms within the unit cell. The impact of uranium (U) and thorium (Th) on the bonding and electronic structure of these compounds can be demonstrated using their charge density distribution. Fig. 8 shows the charge density (e Å^{-3}) distribution for Ru_3B_2X (X = Th, U) in (100), (101), and (110) crystallographic planes. As evident from Fig. 8, in the (100) crystallographic plane, strong Ru–Ru bonding is indicated by the extremely localized charge density around Ru atoms in both compounds. Since the charge is primarily localized close to Ru atoms, the charge density distribution in this plane indicates little interaction with U or Th atoms.

The distinctions between the bonding properties of Ru_3B_2U and Ru_3B_2Th, however, are visible in the (101) and (110) planes. Significant delocalization and overlap between Ru, U, and B atoms are evident in the charge density of Ru_3B_2U, especially in the (110) plane. On the other hand, there is less overlap and a more localized charge density surrounding the Th atoms in the charge density distribution of Ru_3B_2Th. According to this localization, more dispersed electronic orbitals and lower electronegativity of Th than U suggest that it contributes less to bonding interactions. Th and nearby Ru or B atoms have less charge density overlap in the (101) and (110) planes of Ru_3B_2Th, which suggests less Ru–Th and Th–B bonding interactions. While the electrical characteristics of Th are responsible for the decreased bonding strength in Ru_3B_2Th, our results demonstrate the crucial function that U plays in strengthening bonding contacts within Ru_3B_2U. From Fig. 8, it can be clearly seen that charge overlap occurs between Ru and B atoms as well as U/Th and B atoms. This charge sharing is an indication of covalent bonding. So, covalent bonding has greater significance than ionic bonding in both compounds.
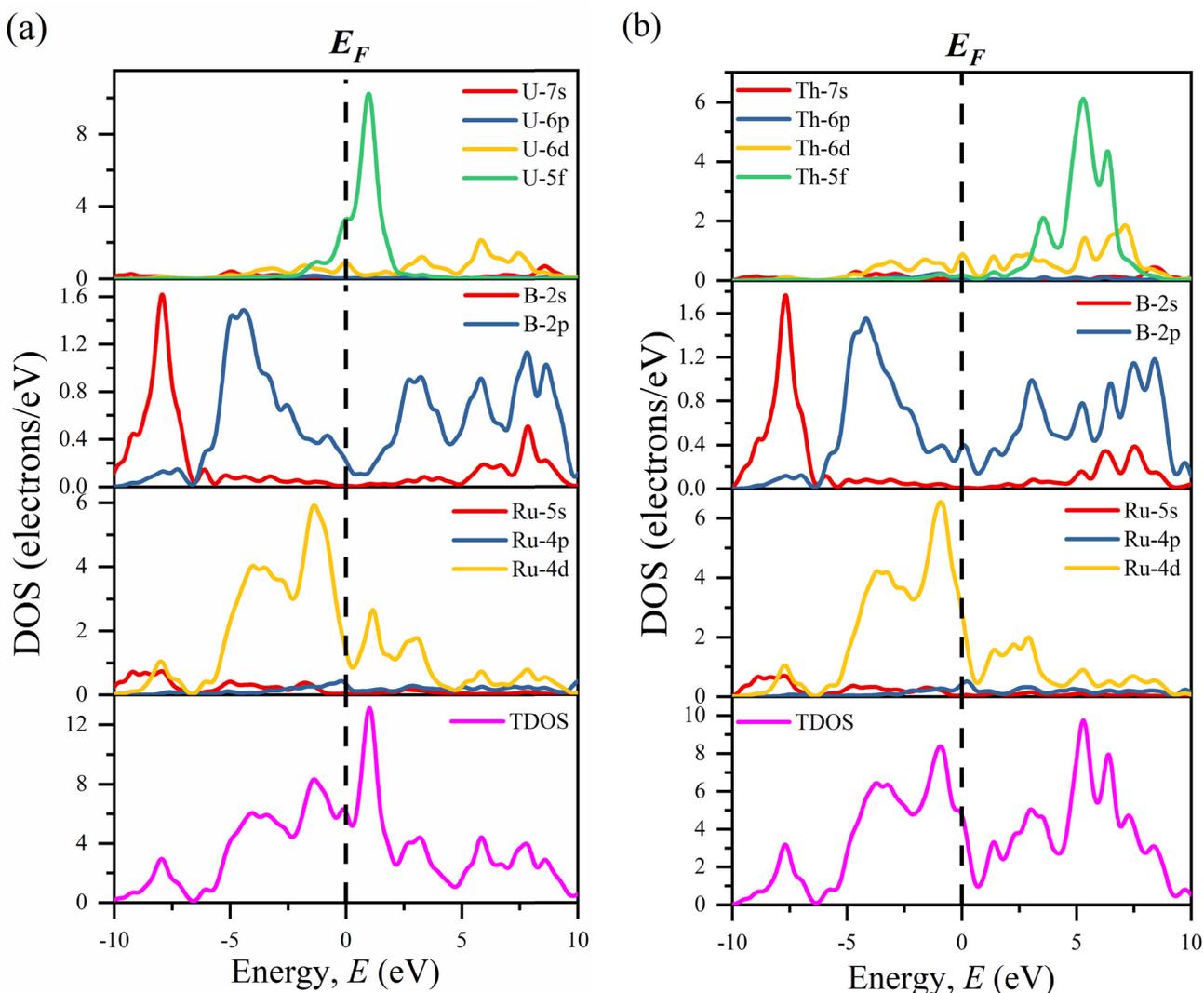
Fig. 6 The partial and total density of states (PDOS and TDOS, respectively) plots of (a) Ru_3B_2U and (b) Ru_3B_2Th as a function of energy.

3.4 Bond population analysis

In order to better understand the bonding nature and electric charge contribution from each atom in Ru_3B_2X (X = Th, U), the Mulliken bond population analysis[67] technique was used. The Mulliken charge measures how the electronic structure varies with atomic displacement and is connected to the vibrational characteristics of molecules.[68] Table 6 shows the charge spilling parameter and atomic charges generated from these computations.

The computation shows that the overall charge of the U and Th atoms is greater than that of any other species present in the compounds Ru_3B_2U and Ru_3B_2Th, respectively. While thorium in Ru_3B_2Th exhibits significantly reduced f-orbital participation (0.46 electrons), resulting in weaker bonds, uranium in Ru_3B_2U has large f-orbital contributions (2.83 electrons), which enhance covalent bonding. Additionally, Ru_3B_2U exhibits superior charge localization and bonding stability, as evidenced by a lower charge spilling parameter (0.17%) than that of Ru_3B_2Th (0.20%). The formal charges that would be predicted for a purely ionic state are all different from these charges. As a result, charge transfers occur between the atoms, and this departure from the formal ionic charge indicates that covalent bonds with an ionic contribution are present.

The effective valence charge (EVC) of a species is the difference between the formal ionic charge and the Mulliken charge of an atom in that substance,[69] which are listed in Table 6. It can be utilized to assess the level of ionicity and covalency. The deviation of EVC from zero refers to the prominent covalent bonding in the Ru_3B_2X (X = Th, U) system. The Hirshfeld population analysis (HPA)[70] produces more significant results as it does not require a reference to the basis set or its location. Compared to those from the Mulliken population analysis, the Hirshfeld charges mentioned in Table 6 are substantially smaller.

The calculated bond overlap population and bond length in Ru_3B_2X (X = Th, U) are summarized in Table 7. The bond overlap population indicates how strong the covalent link is between atoms as well as how strong the bond is per unit
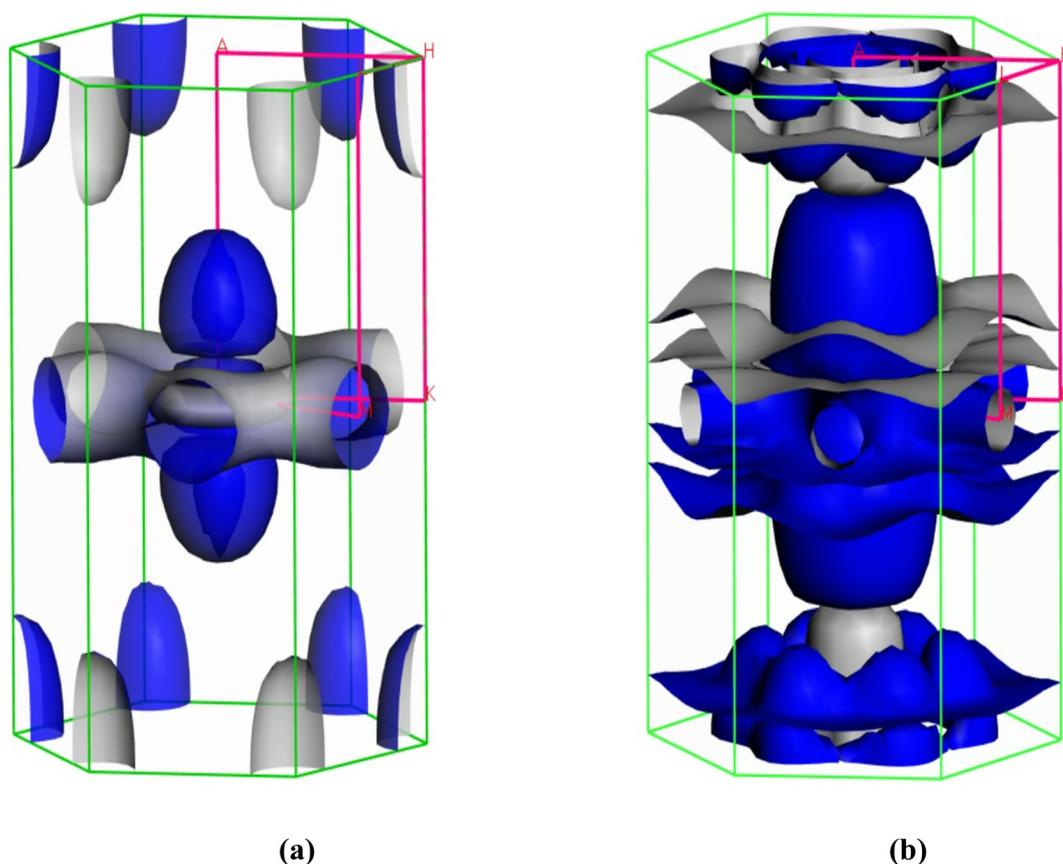
Fig. 7   The Fermi surfaces of (a) Ru_3B_2U and (b) Ru_3B_2Th.

volume. Ru–B bonds have a moderate covalent character, as indicated by their Mulliken overlap population of 0.67 for Ru_3B_2U, whereas the Ru–Ru bonds have a negative overlap population of −0.87, which suggests a net repulsive interaction or antibonding nature. In contrast to Ru_3B_2U, Ru_3B_2Th exhibits a higher negative Ru–Ru overlap population of −1.04, suggesting greater antibonding interactions[71] between Ru atoms, and a somewhat lower Ru–B bond overlap population (0.60), suggesting weaker bonding. Ru_3B_2X exhibits strong covalent Ru–B bonds comparable to TiB_2 (B–B covalent bonds). However, the inclusion of actinides introduces metallic Ru–X interactions (Th/U–Ru bond lengths: ~2.94–3.02 Å), contrasting with purely covalent bonding in B-rich borides like $B_{12}C_3$. The compounds Ru_3B_2U and Ru_3B_2Th also differ in their bond lengths. Stronger Ru–B interactions are indicated by the shorter Ru–B bond length (2.17773 Å) in Ru_3B_2U compared to Ru_3B_2Th (2.22268 Å). Similarly, the Ru–Ru bond length in Ru_3B_2U (2.75411 Å) is slightly shorter than in Ru_3B_2Th (2.78527 Å), consistent with the reduced antibonding interactions in the former. The covalent bonding strength is described by Phillips's homopolar band gap ($E_h = 39.74/d^{2.5}$),[72] which is proportional to the dislocation glide activation energies in polar covalent crystals. d is the bond length and E_h represents the pure covalent contribution (eV) to hardness. The estimated values are displayed in Table 7.

3.5   Acoustic properties

The acoustic properties are an important concern that affects the thermal and electrical conductivity of a material. Effective sound management is essential in safeguarding against sound pollution, thereby requiring the use of a material that allows sound waves to be reflected.[73] The second-order elastic constants provide insights into the propagation of acoustic waves within a substrate. The fundamental acoustic parameters investigated in this work include the velocity of sound and its anisotropy, the impedance of sound, and the coefficient of sound radiation.

Acoustic velocity is the speed at which sound waves propagate when they pass through a solid material, which is determined by the elastic characteristics of the material and can be described using longitudinal velocity (P-wave velocity) and transverse velocity (S-wave velocity). In a crystalline material, the transverse, longitudinal, and mean sound velocities are calculated using the equations provided below:[74]

$$v_t = \sqrt{\frac{G}{\rho}}, \; v_l = \sqrt{\frac{B + 4G/3}{\rho}} \text{ and } v_m = \left[\frac{1}{3}\left(\frac{2}{v_t^3} + \frac{1}{v_l^3}\right)\right]^{-1/3} \quad (19)$$

where the transverse, longitudinal, and mean sound velocities are defined by v_t, v_l, and v_m, respectively. The symbol ρ denotes the mass-density of the crystal. Table 8 presents a
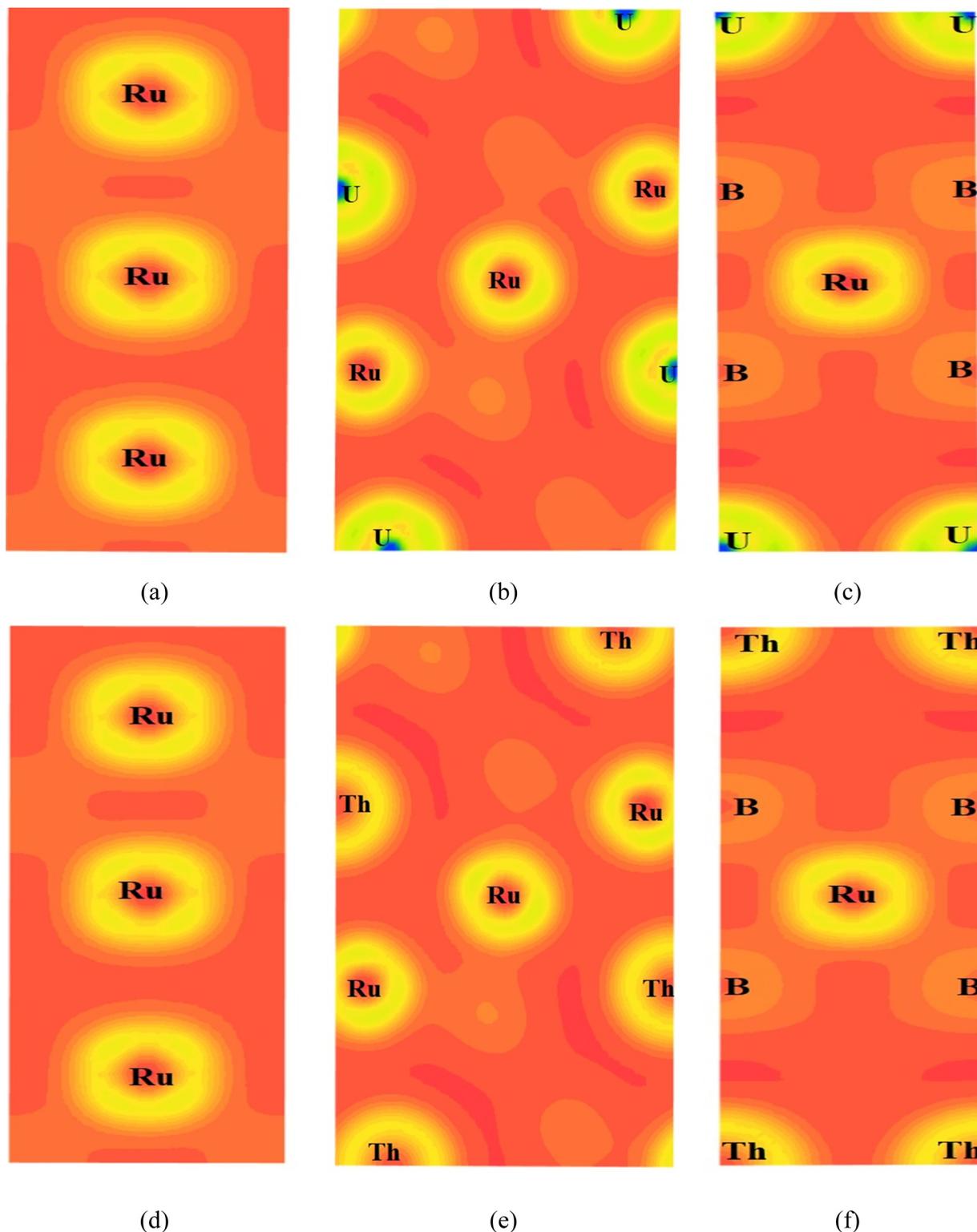
Fig. 8 Electronic charge density distribution of Ru_3B_2U in (a) (100), (b) (101), and (c) (110) planes and Ru_3B_2Th in (d) (100), (e) (101), and (f) (110) planes.

summary of the estimated acoustic velocities. The results of our investigation indicate that Ru_3B_2U exhibits greater hardness than Ru_3B_2Th, as evidenced by its higher sound velocities.

An essential factor that governs the transmission of acoustic energy between two media is the acoustic impedance (Z). The magnitude of sound received and reflected at the interface during the transmission of sound between two substances is

Table 6 Charge spilling parameter (%), orbital charges (electron), atomic Mulliken charges (electron), formal ionic charge (electron), effective valence (electron), and Hirshfeld charge (electron) of different atoms in Ru_3B_2X (X = Th, U)

| Compound | Charge spilling | Species | Mulliken atomic populations | | | | | Mulliken charge | Formal ionic charge | Effective valence | Hirshfeld charge | Effective valence |
			s	P	d	f	Total					
Ru_3B_2U	0.17	Ru	1.03	−0.45	7.18	0	7.76	0.24	+3	2.76	0.10	2.90
		B	1.30	2.41	0	0	3.71	−0.71	−3	2.29	−0.21	2.79
		U	3.23	4.56	2.67	2.83	13.29	0.71	+3	2.29	0.11	2.89
Ru_3B_2Th	0.20	Ru	0.95	−0.60	7.25	0	7.6	0.40	+3	2.60	0.11	2.89
		B	1.31	2.37	0	0	3.68	−0.68	−3	2.32	−0.18	2.82
		Th	2.96	5.79	2.64	0.46	11.85	0.15	+3	2.85	0.05	2.95

Table 7 Calculated Mulliken overlap population P^μ, bond length d^μ (Å), and pure covalent contribution E_h (eV) in Ru_3B_2X (X = Th, U)

Compound	Bond	P^μ	d^μ	E_h
Ru_3B_2U	Ru–B	0.67	2.17773	5.678
	Ru–Ru	−0.87	2.75411	3.157
Ru_3B_2Th	Ru–B	0.60	2.22268	5.395
	Ru–Ru	−1.04	2.78527	3.069

determined by the acoustic impedance difference between the two materials. Hence, when the two impedances are approximately identical, the majority of the sound is conducted. The expression for the acoustic impedance of a solid is given by $Z = \sqrt{\rho G}$, where ρ and G, respectively, represent the density and shear modulus of the medium.[75] Table 8 reports the computed acoustic impedances for Ru_3B_2X (X = Th, U), suggesting that the speed of sound is higher in Ru_3B_2U than in Ru_3B_2Th.

An additional crucial design factor in acoustics is the intensity of sound radiation when designing acoustic insulation and soundproofing materials. For a given driving source, the radiation intensity, I, is directly proportional to the surface velocity. This relationship scales with the modulus of stiffness and density as[76]

$$I = \frac{v}{\rho} = \sqrt{G/\rho^3} \ (\text{m}^4 \ \text{kg}^{-1} \ \text{s}^{-1})$$

where $\sqrt{G/\rho^3}$ is the radiation factor. Instrument manufacturers typically use materials with high radiation factor values to incorporate into appropriately constructed soundboards. In addition, the acoustic conversion efficiency (ACE) of a medium is directly affected by this entity. Table 8 also provides the corresponding predicted radiation factor value for Ru_3B_2X (X = Th, U).

Each atom in a solid has three vibrational modes: two transverse and one longitudinal. Only along specific axes may the pure longitudinal and transverse modes exist in an anisotropic composite. However, in every other direction, the propagating modes are either quasi-longitudinal or quasi-transverse. Only the symmetry directions along [100] and [001] can have pure transverse and longitudinal modes due to the hexagonal symmetry of the compound. The single crystal elastic constants can be used to compute the acoustic velocities of Ru_3B_2X (X = Th, U) in three primary directions:[77]

In the [100] direction,

$$[100]v_l = \sqrt{\frac{(C_{11} - C_{12})}{2\rho}}; \quad [010]v_{t1} = \sqrt{\frac{C_{11}}{\rho}};$$
$$[001]v_{t2} = \sqrt{\frac{C_{44}}{\rho}} \quad (20)$$

In the [001] direction,

$$[001]v_l = \sqrt{\frac{C_{33}}{\rho}}; \quad [100]v_{t1} = [010]v_{t2} = \sqrt{\frac{C_{44}}{\rho}}; \quad (21)$$

where v_{t1} and v_{t2} are the first and second transverse modes, respectively. Inside a material, the velocity of elastic waves is solely determined by the nature of the material itself, not by the size or frequency of the waves. Table 9 contains the estimated sound velocities in various directions, revealing that along both directions, Ru_3B_2U exhibits higher longitudinal and transverse velocities compared to those of Ru_3B_2Th. The strong direction dependence in sound velocities in both compounds suggests that direction dependence is also anticipated in thermal and charge transport parameters.

3.6 Thermophysical properties

Factors such as Debye temperature, melting temperature, thermal conductivity, and thermal expansion coefficient are utilized

Table 8 Transverse sound velocity v_t (ms^{-1}), longitudinal sound velocity v_l (ms^{-1}), average sound wave velocity v_m (ms^{-1}), acoustic impedance Z (Rayl = kg m^{-2} s^{-1}), radiation factor $\sqrt{G/\rho^3}$ (m^4 kg^{-1} s^{-1}), and density ρ (g cm^{-3})

Compound	v_t	v_l	v_m	Z	$\sqrt{G/\rho^3}$	ρ
Ru_3B_2U	3328.86	6015.38	3708.67	39.79	0.279	11.95
Ru_3B_2Th	2880.36	5399.61	3217.76	32.29	0.257	11.21

Table 9 Anisotropic sound velocities (ms^{-1}) of Ru_3B_2X (X = Th, U) along different crystallographic directions

Propagation directions		Ru_3B_2U	Ru_3B_2Th
[100]	$[100]v_l$	3532.87	3022.88
	$[010]v_{t1}$	6237.02	5504.11
	$[001]v_{t2}$	3004.60	2711.19
[001]	$[001]v_l$	6149.94	5425.35
	$[100]v_{t1}$	3004.60	2711.19
	$[010]v_{t2}$	3004.60	2711.19

for assessing the thermal properties of a material. Studying these factors enables the prediction of possible solutions for the system.

3.6.1 Debye temperature. The Debye temperature of a material, one of the most extensively researched physical characteristics in solid-state physics, represents the bonding strength between atoms and their energy of vibration. Crystals exhibit a positive correlation between the Debye temperature and the phonon thermal conductivity, and this temperature differentiates between the classical and quantum-mechanical characteristics of phonon dispersion. Using the elastic constants at low temperatures, the Debye temperature is calculated since vibrational excitations at low temperatures are exclusively induced by acoustic vibrations. The formula for this estimation is[78]

$$\Theta_{\mathrm{D}} = \frac{h}{k_{\mathrm{B}}} \left[\left(\frac{3n}{4\pi V_0} \right) \right]^{1/3} v_{\mathrm{m}} \quad (22)$$

In this context, h represents Planck's constant, k_{B} denotes Boltzmann's constant, V_0 defines the volume of the unit cell, and n specifies the number of atoms in the cell. The high Debye temperature values reported in Table 10 for both Ru_3B_2U and Ru_3B_2Th indicate that certain properties such as high melting point, high thermal conductivity, low specific heat, and high stiffness are anticipated. Moreover, the value of Θ_{D} is sensitive to temperature and decreases as temperature increases, owing to the temperature-dependent nature of elastic constants and sound velocity of the substance. At values below and over Θ_{D}, the acoustic and optical phonon modes are anticipated to be more dominant in the lattice, respectively.

3.6.2 Melting temperature. The comprehension of the melting characteristics of solids holds significant importance in the field of materials science and engineering since it directly impacts the processing and functionality of materials in multiple fields. Specifically, materials with low and high T_{m} are suitable options for thermal interface material (TIM) and thermal barrier coatings, respectively. Using the elastic constants, the melting temperature T_{m} of solids can be determined with the help of the following equation:[79]

$$T_{\mathrm{m}} = 354 \text{ K} + \left(4.5 \text{ K GPa}^{-1}\right)\left(\frac{2C_{11} + C_{33}}{3}\right) \pm 300 \text{ K} \quad (23)$$

The calculated melting points for Ru_3B_2X (X = Th, U) are included in Table 10. Both compounds have extremely high melting temperatures, making them potentially suitable for use in environments with severe thermal conditions. Ru_3B_2U has a

significantly greater melting point in comparison to Ru_3B_2Th. Hence, Ru_3B_2U will exhibit superior bonding and cohesive energy in comparison to Ru_3B_2Th. It is worth noting that the melting temperature rises in proportion to the bonding strength, enhanced cohesive energy, and reduced coefficient of thermal expansion.[80]

3.6.3 Thermal expansion coefficient and heat capacity. The thermal expansion coefficient (α) of a material is a physical characteristic that quantifies the extent to which its dimensions alter in reaction to a temperature change and relate to the anharmonic lattice vibrations. The suitability of a material for use as a thermal barrier coating (TBC) material is closely controlled by this property. Furthermore, it measures several characteristics of a substance, including thermal conductivity, specific heat, entropy, and isothermal compressibility. The thermal expansion coefficient of a material can be determined by utilizing the shear modulus G, which is given $\alpha = (1.6 \times 10^{-3})/G$,[81] and the computed values for Ru_3B_2X (X = Th, U) are presented in Table 10. The estimated values suggest that Ru_3B_2Th experiences a significant expansion compared to Ru_3B_2U when heated and contracts when cooled. Additionally, an inverse relationship exists between α of a material and its melting temperature ($\alpha = 0.02/T_{\mathrm{m}}$).[82]

Another crucial thermophysical characteristic is the heat capacity per unit volume (ρC_{P}), which is sometimes referred to as volumetric heat capacity. The alteration in heat energy per unit volume in a material due to a temperature change of one Kelvin is referred to as ρC_{P} of the substance, and is calculated by $\rho C_{\mathrm{P}} = 3k_{\mathrm{B}}/\Omega$.[81] Here, the number of atoms per unit volume is denoted as $N = 1/\Omega$. The thermal energy storage capacity and thermal sensitivity to temperature variations of a material are quantified by this measurement. Table 10 also lists the calculated values of heat capacity per unit volume of Ru_3B_2X (X = Th, U).

3.6.4 Wavelength of the dominant phonon. Quantum lattice vibrations of materials, known as phonons, have a substantial impact on several physical properties including electrical conductivity, thermal conductivity, and heat capacity. The dominant phonon wavelength (λ_{dom}) is the wavelength where the phonon distribution function reaches its peak. An estimation of the wavelength of the dominating phonon for Ru_3B_2X (X = Th, U) at 300 K has been obtained using the following relationship:[82]

$$\lambda_{\mathrm{dom}} = \frac{12.566 v_{\mathrm{m}}}{T} \times 10^{-12} \quad (24)$$

where v_{m} represents the mean sound velocity in meters

Table 10 The Debye temperature Θ_{D} (K), melting temperature T_{m} (K), thermal expansion coefficient α (K^{-1}), heat capacity per unit volume ρC_{P} (J m^{-3} K^{-1}), the wavelength of the dominant phonon at 300 K λ_{dom} (m), Grüneisen parameter γ, minimum thermal conductivity k_{min} (W m^{-1} K^{-1}), and lattice thermal conductivity k_{ph} (W m^{-1} K^{-1})

Compound	Θ_{D}	T_{m}	α ($\times 10^{-5}$)	ρC_{P} ($\times 10^6$)	λ_{dom} ($\times 10^{-12}$)	γ	k_{min}	k_{ph}[a]
Ru_3B_2U	469.41	2426.53	1.21	3.18	155.34	1.65	0.925	26.579
Ru_3B_2Th	400.11	1867.77	1.72	3.01	134.71	1.78	0.774	14.071

[a] Measured at 300 K.

per second, while T denotes the temperature in Kelvin. The measured value of λ_{dom} (Table 10) for Ru_3B_2X (X = Th, U) indicates that the phonon distribution function peaks at a higher wavelength in the case of Ru_3B_2U compared to Ru_3B_2Th.

3.6.5   Grüneisen parameter. In general, the Grüneisen parameter (γ) is a function of both volume and temperature and is directly connected to the strength of phonon–phonon interaction. This parameter describes several characteristics of a material, including thermal conductivity and expansion, the relation between temperature and elastic properties, attenuation of acoustic waves, and the anharmonicity of the bonds in a crystal. The calculation of the Grüneisen parameter γ, for Ru_3B_2X (X = Th, U), has been performed using the following equation:

$$\gamma = \frac{3}{2}\left(\frac{1+\nu}{2-3\nu}\right) \quad (25)$$

where ν is the Poisson ratio. The calculated values of γ for Ru_3B_2X (X = Th, U) (Table 10) indicate the presence of significant anharmonicity, implying that the thermal conductivity of both compounds is poor. Moreover, a high value of γ indicates that the thermal characteristics of the compound, including thermal expansion, specific heat, and thermal conductivity, are very responsive to variations in temperature and pressure.

3.6.6   Minimum and lattice thermal conductivity. Finding and developing materials that can be used as TBC (thermal barrier coating) materials has been greatly aided by studies on the lowest phonon thermal conductivity that a material can display at high temperatures. The minimum thermal conductivity k_{min} of Ru_3B_2X (X = Th, U) at high temperatures can be determined using Clarke's formula as follows:[82]

$$k_{min} = k_B v_m \left(\frac{nN_A\rho}{M}\right)^{2/3} \quad (26)$$

where k_B is the Boltzmann constant, v_m is the average sound velocity, n is the number of atoms in a molecule, N_A is Avogadro's number, ρ is the mass density, and the molecular weight is denoted by M. Both compounds have relatively low k_{min} values, which are shown in Table 10. It is important to remember that materials with very poor heat conductivity might find practical uses in thermoelectric devices or insulation. Ru_3B_2X (X = Th, U) compounds can be utilized as TBC materials at ambient pressure, as the k_{min} of these compounds is less than the limitation value of 1.25 W m^{-1} K^{-1}.[83]

On the flip side, the contribution of phonons to the total thermal conductivity of a material is known as lattice thermal conductivity, k_{ph}. It illustrates how the propagation of phonons causes heat to be efficiently transferred through a material. The following empirical formula, developed by Slack,[84] was used in this investigation to determine the k_{ph} of Ru_3B_2X (X = Th, U) compounds at room temperature and the results are shown in Table 10:

$$k_{ph} = A(\gamma)\frac{M_{av}\Theta_D^3\delta}{\gamma^2 n^{2/3} T} \quad (27)$$

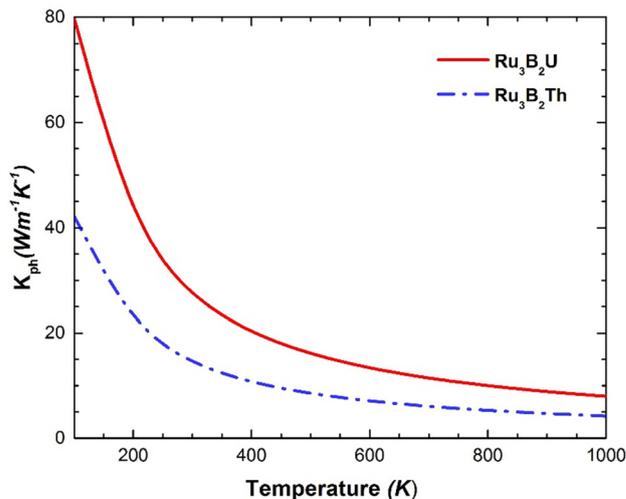**Table 11** Lattice thermal conductivity k_{ph} (W m^{-1} K^{-1}) at various temperatures

Temperature (K)	Ru$_3$B$_2$U	Ru$_3$B$_2$Th
100	79.738	42.213
200	39.869	21.107
300	26.579	14.071
400	19.935	10.553
500	15.948	8.443
600	13.290	7.036
700	11.391	6.030
800	9.967	5.277
900	8.860	4.690
1000	7.974	4.221

where M_{av} stands for the average atomic mass, Θ_D is the Debye temperature, δ refers to the cubic root of the average atomic volume, γ is the Grüneisen parameter, n denotes the total number of atoms in the unit cell, and T stands for the absolute temperature. The factor $A(\gamma)$ is determined by Julian's formula:[85]

$$A(\gamma) = \frac{5.72 \times 10^7 \times 0.849}{2 \times \left(1 - \frac{0.514}{\gamma} + \frac{0.228}{\gamma^2}\right)} \quad (28)$$

The low k_{ph} values of Ru_3B_2Th compared to that of Ru_3B_2U imply that Ru_3B_2Th can be employed more effectively for thermal insulation than Ru_3B_2U. The temperature variations of the lattice thermal conductivity of both compounds are listed in Table 11. Also, Fig. 9 shows that the bonding and atomic characteristics of U and Th have a considerable impact on lattice thermal conductivity. Because of the stronger covalent bonding involving U, which reduces phonon dispersion and improves heat transmission, Ru_3B_2U shows noticeably higher k_{ph} at any particular temperature than Ru_3B_2Th. As the temperature rises, the k_{ph} of Ru_3B_2X (X = Th, U) falls, which is consistent with normal phonon scattering behavior. These

Fig. 9 Variation of lattice thermal conductivity of Ru_3B_2X (X = Th, U) as a function of temperature.

distinctions suggest that Ru_3B_2Th may be more appropriate for applications where thermal insulation is desired.

3.7 Optical properties

The optical properties are the result of interactions between the photons in light impacting the surface of a material and the charge carriers. The specifics of the electronic band structure of a material have a significant influence on the frequency- and energy-dependent factors that define the optical response of the material. For two distinct polarization orientations [100] and [001], the dielectric function $\varepsilon(\omega)$, absorption coefficient $\alpha(\omega)$, reflectivity $R(\omega)$, refractive index $n(\omega)$, optical conductivity $\sigma(\omega)$, and energy loss function $L(\omega)$ of Ru_3B_2X (X = Th, U) were examined as a function of photon energies up to 40 eV. The necessary equations to calculate these optical properties can be found in the literature.[86,87] The metallic character of the substance under investigation has led to the application of the

Drude damping parameter of 0.5 eV[88,89] with an energy smearing of 0.5 eV.

The complex-valued dielectric function, $\varepsilon(\omega) = \varepsilon_1(\omega) + \varepsilon_2(\omega)$, represents how a material reacts to an external electric field. The real and imaginary components of $\varepsilon(\omega)$ are $\varepsilon_1(\omega)$ and $\varepsilon_2(\omega)$, respectively. The electric polarization that occurs when light passes through a medium is explained by the real part $\varepsilon_1(\omega)$. With a strong Drude peak at low energy, the real part, $\varepsilon_1(\omega)$ in Fig. 10(a), exhibits metallic characteristics. It has a prominent peak in the range of 0–0.6 eV and falls below zero at ~ 0.6 eV for both compounds. It stays below the zero level until ~ 30.5 eV and ~ 29.2 eV are reached for Ru_3B_2U and Ru_3B_2Th, respectively. Conversely, the imaginary component, $\varepsilon_2(\omega)$, corresponds to absorption characteristics and the electronic band structure of a material. As seen in Fig. 10(b), the value of $\varepsilon_2(\omega)$ is highest at zero energy and decreases as photon energy increases, a behavior which is fairly frequent in metallic systems. An energy range where the imaginary part is nonzero
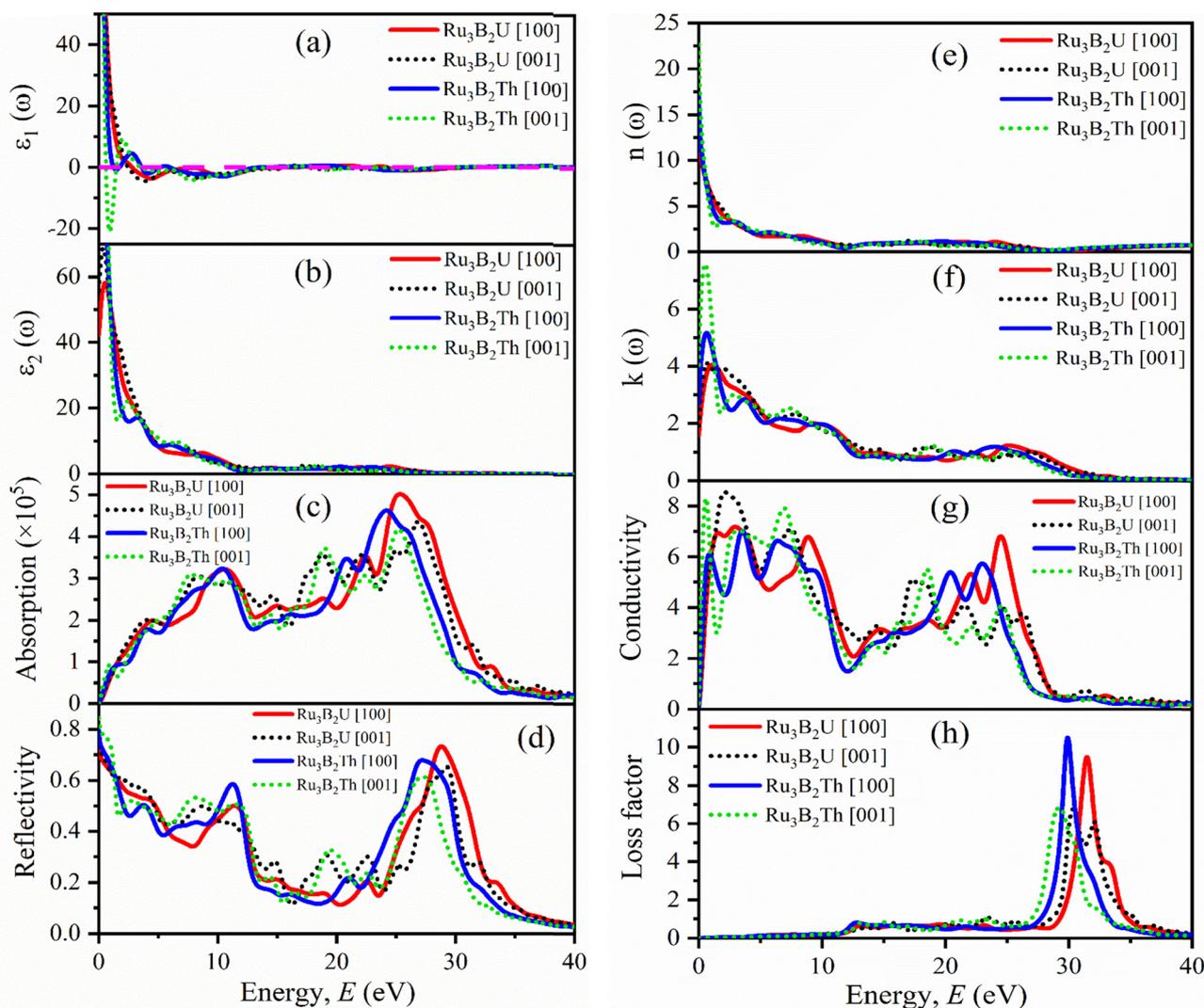
Fig. 10 (a) $\varepsilon_1(\omega)$, (b) $\varepsilon_2(\omega)$, (c) absorption coefficient, (d) reflectivity, (e) $n(\omega)$, (f) $k(\omega)$, (g) optical conductivity, and (h) energy loss function of Ru_3B_2X (X = Th, U) in the [001] and [100] direction.

indicates that the photons are absorbed by a material. The figures reveal that for Ru_3B_2U and Ru_3B_2Th, the value of $\varepsilon_2(\omega)$ becomes zero at about 29.5 eV and 27.9 eV, respectively, indicating that the compounds will exhibit transparency above that energy value. In the low energy range, there is anisotropy in both real and imaginary components.

The absorption spectra $\alpha(\omega)$ of Ru_3B_2X (X = Th, U) as a function of photon energy for [100] and [001] polarizations are shown in Fig. 10(c). The fact that the absorption begins at 0 eV in both situations is additional evidence of their metallic nature. As we can see from this figure, the absorption fluctuates significantly within the 5–20 eV energy range. For [001] and [100] polarization directions, the maximum light absorption of Ru_3B_2U occurs at approximately 26.8 eV and 25.3 eV, respectively, whereas the maximum light absorption of Ru_3B_2Th for the [001] and [100] polarization directions occurs at roughly 25.2 eV and 24.2 eV, respectively. A sharp decline in absorption occurs following the position of these peaks. Notably, the absorption coefficient of Ru_3B_2X (X = Th, U) is high enough for it to be used as a good solar absorber in photovoltaic device applications.

With respect to photon energy, the reflectivity spectra of Ru_3B_2X (X = Th, U) are shown in Fig. 10(d), which represent the ratio of photon energy that is incident to that is reflected. These spectra start from zero photon energy with 74% and 79% for Ru_3B_2X (X = Th, U), respectively. Reflectivity decreases sharply for all samples around 10 eV but shows a slight increase at higher energies (above 20 eV). Also, there is a clear optical anisotropy in the reflectivity spectra. Ru_3B_2X shows high IR reflectivity ($>70\%$), outperforming traditional IR reflectors like Au or Al. This property aligns with metallic borides (e.g., ZrB_2) but with improved anisotropy due to hexagonal symmetry.

An expression for the complex refractive index of a material is $N(\omega) = n(\omega) + ik(\omega)$, where $k(\omega)$ is the extinction coefficient which is an extensively researched parameter in the construction of optoelectronic devices. Fig. 10(e) and (f) show the refractive index of Ru_3B_2X (X = Th, U) as a function of photon energy, acquired in two polarization directions. The low energy IR and visible regions have a relatively high refractive index which refers to the compounds that can be used as a waveguide and in photonic engineering. Also, the extinction coefficient of both the compounds exhibits peaks in the same energy region. Comparable peaks in the imaginary component of the dielectric function can be detected in such low energy regions implying that both the refractive index and extinction coefficient are connected to photon energy loss.

In the presence of an alternating electric field, the optical conductivity of a material is another extensively researched property that indicates its ability to conduct electricity. Fig. 10(g) displays the photoconductivity $\sigma(\omega)$ of Ru_3B_2X (X = Th, U) for both [100] and [001] polarizations. Photoconductivity beginning with zero photon energy is a sign of the absence of an electronic band gap. Conductivity varies significantly across the energy range and several peaks occur at distinct energy values. These peaks might correspond to electronic transition or interaction between energy states which are affected by

material types and their anisotropy. The conductivity of a material is also significantly influenced by the number of free charge carriers that have the ability to conduct electricity. Over 30 eV, the optical conductivity of Ru_3B_2X (X = Th, U) becomes isotropic for both the polarization directions.

Fig. 10(h) shows the electron energy loss spectrum as a function of frequency for Ru_3B_2X (X = Th, U), which is related to its absorption and reflection characteristics. It is evident from the figure that neither compound loses energy up to roughly 12 eV due to the comparatively high value of $\varepsilon_2(\omega)$. The maximum energy loss is observed for Ru_3B_2U at around 33 eV whereas for Ru_3B_2Th, a similar peak is found at nearly the same position but with slightly lower energy. The compound Ru_3B_2U shows higher loss than Ru_3B_2Th, indicating greater energy dissipation in U-doped samples. The sharp peak in the loss factor corresponds to specific plasmon resonance energies and hence the bulk plasma frequency ω_p can be found from the energy loss spectrum.[86]

4. Conclusion

The ground-state characteristics of ternary borides Ru_3B_2X (X = Th, U) are thoroughly examined in this work using first-principles density functional theory (DFT) computations. In agreement with experimental findings, our structural analysis showed that Ru_3B_2U and Ru_3B_2Th crystallize in a hexagonal configuration and also that the lattice constants and unit cell volumes closely resemble previously published experimental results, proving the accuracy of our methodology. Both structures are found to be stable. Higher values of elastic moduli reveal that Ru_3B_2U exhibits superior stiffness and resilience. Despite the fact that both materials are ductile, Poisson's and Pugh's ratios support the slightly higher ductility of Ru_3B_2Th. In contrast, Ru_3B_2U shows increased mechanical anisotropy, indicating direction-dependent mechanical behavior.

The presence of bands that pass the Fermi level in electronic structure calculations supports that both compounds are metallic. Because Ru_3B_2Th has a greater density of states at the Fermi level, it demonstrated stronger metallic behavior. The bonding study of Ru_3B_2U demonstrated significant hybridization between Ru-4d states and B-2p states, indicating better covalent interactions. The mechanical strength of Ru_3B_2U is further highlighted by acoustic qualities obtained from elastic constants, which include higher sound velocities and acoustic impedance values. Its increased hardness and fracture toughness suggest potential uses in situations that can withstand wear.

Ru_3B_2U exhibits better thermal stability and performance in harsh environments because of its higher Debye temperature, melting temperature, and lower thermal expansion coefficient. Ru_3B_2Th, on the other hand, has the potential to be used as a thermal barrier coating material due to its reduced lattice thermal conductivity. High reflectivity in the visible spectrum was found when the optical characteristics of Ru_3B_2X (X = Th, U) were examined, indicating possible uses in optical coatings

and display technology, especially in the IR region. Both Ru_3B_2U and Ru_3B_2Th can be used as efficient materials for optical devices, according to the computed dielectric function and refractive index, with Ru_3B_2Th showing somewhat higher reflectivity. These findings open the door for additional experimental research and technical developments in the fields of aerospace, thermal management, and superconducting materials by offering insightful information on the functional potential of Ru_3B_2X (X = Th, U) compounds.

Data availability

The data supporting this article have been included as part of the ESI.†

Conflicts of interest

The authors declare that they have no known competing financial interests or personal relationships that could have appeared to influence the work reported in this paper.

Acknowledgements

References

1 I. P. Borovinskaya, A. A. Gromov, E. A. Levashov, Y. M. Maksimov, A. S. Mukasyan and A. S. Rogachev, *Concise encyclopedia of self-propagating high-temperature synthesis: History, theory, technology, and products*, Elsevier, Amsterdam, 2017, pp. 39–41, DOI: 10.1016/B978-0-12-804173-4.00017-X.

2 J. M. Nsanzimana, R. Dangol, V. Reddu, S. Duo, Y. Peng, K. N. Dinh, Z. Huang, Q. Yan and X. Wang, Facile synthesis of amorphous ternary metal borides–reduced graphene oxide hybrid with superior oxygen evolution activity, *ACS Appl. Mater. Interfaces*, 2018, **11**, 846–855.

3 H. Nowotny, Crystal chemistry of complex carbides and related compounds, *Angew. Chem., Int. Ed. Engl.*, 1972, **11**, 906–915.

4 S. Carenco, D. Portehault, C. Boissiere, N. Mezailles and C. Sanchez, Nanoscaled metal borides and phosphides: recent developments and perspectives, *Chem. Rev.*, 2013, **113**, 7981–8065.

5 J. M. Leitnaker, *Thermodynamic properties of refractory borides: Evaporation behavior and vapor pressure of zirconium diboride. Phase studies in the tantalum-boron system between Ta and TaB*, Los Alamos Scientific Laboratory of the University of California, 1960, vol. 2402.

6 J. M. Leitnaker, N. H. Krikorian and M. G. Bowman, *High temperature poisons*, Los Alamos Scientific Lab., N. Mex., 1961.

7 J. M. Leitnaker, N. H. Krikorian and M. C. Krupka, Unusual ternary behavior of transition metal borides, *J. Electrochem. Soc.*, 1962, **109**, 66.

8 A. N. Kolmogorov, M. Calandra and S. Curtarolo, Thermodynamic stabilities of ternary metal borides: an ab initio guide for synthesizing layered superconductors, *Phys. Rev. B: Condens. Matter Mater. Phys.*, 2008, **78**, 094520.

9 K. Togano, P. Badica, Y. Nakamori, S. Orimo, H. Takeya and K. Hirata, Superconductivity in the metal rich Li–Pd–B ternary boride, *Phys. Rev. Lett.*, 2004, **93**, 247004.

10 V. Dhand, J. Lim, S. Bharadwaj, S. Kim and K. Rhee, Sol–gel combustion derived novel ternary transition metal boride-anisotropic magnetic powders and their magnetic property, *J. Mater. Res. Technol.*, 2023, **24**, 7219–7228.

11 A. Ch, Ceramic armor materials by design, *J. Am. Ceram. Soc.*, 2002, 487–489.

12 Z. Zachariev, New superhard ternary borides in composite materials, *Met., Ceram. Polym. Compos. Var. Uses*, 2011, 61–78.

13 B. T. Matthias, E. Corenzwit, J. M. Vandenberg and H. E. Barz, High superconducting transition temperatures of new rare earth ternary borides, *Proc. Natl. Acad. Sci. U. S. A.*, 1977, **74**, 1334–1335.

14 D. C. Johnston, Superconductivity in a new ternary structure class of boride compounds, *Solid State Commun.*, 1977, **24**, 699–702.

15 J. M. Vandenberg and B. T. Matthias, Crystallography of new ternary borides, *Proc. Natl. Acad. Sci. U. S. A.*, 1977, **74**, 1336–1337.

16 P. Rogl, Ternäre Metallboride. [La, Ce, Pr, Nd, Sm] Os_4B_4 und [Y, La, Ce, Pr, Nd, Sm, Gd, Tb] Ir_4B_4 mit $NdCo_4B_4$-Struktur, *Monatsh. Chem.*, 1979, **110**, 235–243.

17 H. C. Ku, G. P. Meisner, F. Acker and D. C. Johnston, Superconducting and magnetic properties of new ternary borides with the $CeCo_3B_2$-type structure, *Solid State Commun.*, 1980, **35**, 91–96.

18 K. Hiebl, P. Rogl, E. Uhl and M. J. Sienko, Magnetic behavior and structural chemistry of $RERu_3B_2$ borides, *Inorg. Chem.*, 1980, **19**, 3316–3320.

19 P. Rogl, The crystal structure of URu_3B_2, *J. Nucl. Mater.*, 1980, **92**, 292–298.

20 E. Burzo, *Rare Earths-Transition Metals-Boron Compounds: Basic Properties to Technical Applications*, Springer Nature, 2023.

21 S. J. Clark, M. D. Segall, C. J. Pickard, P. J. Hasnip, M. J. Probert, K. Refson and M. C. Payne, First principles methods using CASTEP, *Z. Kristallogr.*, 2005, **220**, 567.

22 R. G. Parr, Density functional theory, *Electron Distributions and the Chemical Bond*, Springer US, Boston, MA, 1982, pp. 95–100, DOI: 10.1146/annurev.pc.34.100183.003215.

23 J. P. Perdew, K. Burke and M. Ernzerhof, Generalized gradient approximation made simple, *Phys. Rev. Lett.*, 1996, **77**, 3865.

24 D. Vanderbilt, Soft self-consistent pseudopotentials in a generalized eigenvalue formalism, *Phys. Rev. B: Condens. Matter Mater. Phys.*, 1990, **41**, 7892.

25 H. J. Monkhorst and J. D. Pack, Special points for Brillouin-zone integrations, *Phys. Rev. B: Condens. Matter Mater. Phys.*, 1976, **13**, 5188.

26 T. H. Fischer and J. Almlof, General methods for geometry and wave function optimization, *J. Phys. Chem.*, 1992, **96**, 9768–9774.

27 J. P. Watt, Hashin–Shtrikman bounds on the effective elastic moduli of polycrystals with orthorhombic symmetry, *J. Appl. Phys.*, 1979, **50**, 6290–6295.

28 L. S. Combes, S. S. Ballard and K. A. McCarthy, Mechanical and thermal properties of certain optical crystalline materials, *JOSA*, 1951, **41**, 215–222.

29 A. H. Reshak, V. V. Atuchin, S. Auluck and I. V. Kityk, First and second harmonic generation of the optical susceptibilities for the non-centro-symmetric orthorhombic $AgCd_2GaS_4$, *J. Phys.: Condens. Matter*, 2008, **20**, 325234.

30 S. Saha, T. P. Sinha and A. Mookerjee, Electronic structure, chemical bonding, and optical properties of paraelectric $BaTiO_3$, *Phys. Rev. B: Condens. Matter Mater. Phys.*, 2000, **62**, 8828.

31 G. Kresse and J. Furthmüller, Efficient iterative schemes for ab initio total-energy calculations using a plane-wave basis set, *Phys. Rev. B: Condens. Matter Mater. Phys.*, 1996, **54**, 11169–11186, DOI: 10.1103/PhysRevB.54.11169.

32 G. Kresse and J. Furthmüller, Efficiency of ab initio total energy calculations for metals and semiconductors using a plane-wave basis set, *Comput. Mater. Sci.*, 1996, **6**, 15–50, DOI: 10.1016/0927-0256(96)00008-0.

33 V. Wang, N. Xu, J.-C. Liu, G. Tang and W.-T. Geng, VASPKIT: a user-friendly interface facilitating high-throughput computing and analysis using VASP code, *Comput. Phys. Commun.*, 2021, **267**, 108033, DOI: 10.1016/j.cpc.2021.108033.

34 F. Mouhat and F. X. Coudert, Necessary and sufficient elastic stability conditions in various crystal systems, *Phys. Rev. B: Condens. Matter Mater. Phys.*, 2014, **90**, 224104.

35 M. Born, On the stability of crystal lattices. I, *Math. Proc. Cambridge Philos. Soc.*, 1940, **36**, 160–172.

36 W. Kim, Strategies for engineering phonon transport in thermoelectrics, *J. Mater. Chem. C*, 2015, **3**, 10336–10348.

37 W. Voigt, *Lehrbuch der Kristallphysik: (mit Ausschluss der Kristalloptik)*, B.G. Teubner, 1910.

38 A. Reuß, Berechnung der Fließgrenze von Mischkristallen auf Grund der Plastizitätsbedingung für Einkristalle, *J. Appl. Math. Mech.*, 1929, **9**, 49–58.

39 R. Hill, The elastic behaviour of a crystalline aggregate, *Proc. Phys. Soc., London, Sect. A*, 1952, **65**, 349.

40 R. Hill, Elastic properties of reinforced solids: some theoretical principles, *J. Mech. Phys. Solids*, 1963, **11**, 357–372.

41 M. T. Nasir, M. A. Hadi, M. A. Rayhan, M. A. Ali, M. M. Hossain, M. Roknuzzaman and K. Ostrikov, First-principles study of superconducting ScRhP and ScIrP pnictides, *Phys. Status Solidi B*, 2017, **254**, 1700336.

42 X. Zhan, Z. Li, B. Liu, J. Wang, Y. Zhou and Z. Hu, Theoretical prediction of elastic stiffness and minimum lattice thermal conductivity of $Y_3Al_5O_{12}$, $YAlO_3$, and $Y_4Al_2O_9$, *J. Am. Ceram. Soc.*, 2012, **95**, 1429–1434.

43 P. Mondal, M. R. Islam, M. S. Khanom and F. Ahmed, The impact of hydrostatic pressure on the structural, mechanical, thermal, and optoelectronic characteristics of the RbV_3Sb_5 Kagome compound: ab initio approach, *ChemistryOpen*, 2024, e202400291.

44 M. W. Qureshi, X. Ma, G. Tang and R. Paudel, Structural stability, electronic, mechanical, phonon, and thermodynamic properties of the M_2GaC (M = Zr, Hf) MAX phase: an AB initio calculation, *Materials*, 2020, **13**, 5148.

45 B. G. Pfrommer, M. Côté, S. G. Louie and M. L. Cohen, Relaxation of crystals with the quasi-Newton method, *J. Comput. Phys.*, 1997, **131**, 233–240.

46 O. L. Anderson and H. H. Demarest Jr, Elastic constants of the central force model for cubic structures: polycrystalline aggregates and instabilities, *J. Geophys. Res.*, 1971, **76**, 1349–1369.

47 M. E. Eberhart and T. E. Jones, Cauchy pressure and the generalized bonding model for nonmagnetic bcc transition metals, *Phys. Rev. B: Condens. Matter Mater. Phys.*, 2012, **86**, 134106.

48 W. Feng and S. Cui, Mechanical and electronic properties of Ti_2AlN and Ti_4AlN_3: a first-principles study, *Can. J. Phys.*, 2014, **92**, 1652–1657.

49 L. Kleinman, Deformation potentials in silicon. I. Uniaxial strain, *Phys. Rev.*, 1962, **128**, 2614.

50 M. S. Sorker, M. R. Islam, A. Chakraborty and M. A. Razzak Sarker, First-principles and experimental study to investigate structural, elastic, electronic, thermal, and optical properties of $KCdCl_3$ metal halide perovskite crystals, *AIP Adv.*, 2024, **14**, 4.

51 R. C. Lincoln, K. M. Koliwad and P. B. Ghate, Morse-potential evaluation of second-and third-order elastic constants of some cubic metals, *Phys. Rev.*, 1967, **157**, 463.

52 K. J. Puttlitz and K. A. Stalter, *Handbook of lead-free solder technology for microelectronic assemblies*, CRC Press, 2004.

53 H. Niu, S. Niu and A. R. Oganov, Simple and accurate model of fracture toughness of solids, *J. Appl. Phys.*, 2019, **125**, 6.

54 M. A. Ali, M. M. Hossain, M. M. Uddin, M. A. Hossain, A. K. M. A. Islam and S. H. Naqib, Physical properties of new MAX phase borides M_2SB (M = Zr, Hf, Nb) in comparison with conventional MAX phase carbides M_2SC (M = Zr, Hf, Nb): comprehensive insights, *J. Mater. Res. Technol.*, 2021, **11**, 1000–1018.

55 P. Ravindran, L. Fast, P. A. Korzhavyi, B. Johansson, J. Wills and O. Eriksson, Density functional theory for calculation of elastic properties of orthorhombic crystals: application to $TiSi_2$, *J. Appl. Phys.*, 1998, **84**, 4891–4904.

56 H. Y. Yan, M. G. Zhang, D. H. Huang and Q. Wei, First-principles study of elastic and thermodynamic properties of orthorhombic OsB_4 under high pressure, *Solid State Sci.*, 2013, **18**, 17–23.

57 S. I. Ranganathan and M. Ostoja-Starzewski, Universal elastic anisotropy index, *Phys. Rev. Lett.*, 2008, **101**, 055504.

58 C. M. Kube and M. De Jong, Elastic constants of polycrystals with generally anisotropic crystals, *J. Appl. Phys.*, 2016, **120**, 165105.

59 *Anisotropy in Single-Crystal Refractory Compounds*, ed. F. Vahldiek, Springer, 2013.

60 D. H. Chung and W. R. Buessem, The elastic anisotropy of crystals, *J. Appl. Phys.*, 1967, **38**, 2010–2012.

61 V. Milman and M. C. Warren, Elasticity of hexagonal BeO, *J. Phys.: Condens. Matter*, 2001, **13**, 241.

62 R. Gaillac, P. Pullumbi and F. X. Coudert, ELATE: an open-source online application for analysis and visualization of elastic tensors, *J. Phys.: Condens. Matter*, 2016, **28**, 275201.

63 S. Kerdsongpanya, B. Alling and P. Eklund, Effect of point defects on the electronic density of states of ScN studied by first-principles calculations and implications for thermo-electric properties, *Phys. Rev. B: Condens. Matter Mater. Phys.*, 2012, **86**, 195140.

64 T. Hong, T. J. Watson-Yang, A. J. Freeman, T. Oguchi and J. H. Xu, Crystal structure, phase stability, and electronic structure of Ti–Al intermetallics: TiAl₃, *Phys. Rev. B: Condens. Matter Mater. Phys.*, 1990, **41**, 12462.

65 K. H. Bennemann and J. W. Garland, Theory for super-conductivity in d-band metals, *AIP Conf. Proc.*, 1972, **4**, 103–137.

66 P. Cudazzo, G. Profeta, A. Sanna, A. Floris, A. Continenza, S. Massidda and E. K. U. Gross, Ab initio description of high-temperature superconductivity in dense molecular hydrogen, *Phys. Rev. Lett.*, 2008, **100**, 257001.

67 R. S. Mulliken, Electronic population analysis on LCAO–MO molecular wave functions. I, *J. Chem. Phys.*, 1955, **23**, 1833–1840.

68 P. Mondal, K. Hossain, M. S. Khanom, M. K. Hossain and F. Ahmed, First-principles calculations to investigate structural, elastic, thermodynamic, electronic, and optical properties of AgXCl₃ (X = Fe, Co & Mn), *Comput. Condens. Matter*, 2023, **37**, e00860.

69 M. A. Hadi, S. H. Naqib, S. R. Christopoulos, A. Chroneos and A. K. M. A. Islam, Mechanical behavior, bonding nature and defect processes of Mo₂ScAlC₂: a new ordered MAX phase, *J. Alloys Compd.*, 2017, **724**, 1167–1175.

70 F. L. Hirshfeld, Bonded-atom fragments for describing molecular charge densities, *Theor. Chim. Acta*, 1977, **44**, 129–138.

71 R. D. Harcourt, Diatomic antibonding σ^* s orbitals as 'metallic orbitals' for electron conduction in alkali metals, *J. Phys. B: At. Mol. Phys.*, 1974, **7**, L41.

72 V. K. Srivastava, Ionic and covalent energy gaps of CsCl crystals, *Phys. Lett. A*, 1984, **102**, 127–129.

73 P. Mondal, S. Khanom, N. A. Shahed, M. K. Hossain and F. Ahmed, An ab initio insight into the structural, physical, thermodynamic and optoelectronic properties of superconducting Heusler-like LiGa₂Rh, *Phys. C*, 2022, **603**, 1354142.

74 E. Schreiber, O. L. Anderson and N. Soga, *Elastic constants and their measurement*, McGraw-Hill, 1974.

75 A. Chakraborty, M. N. H. Liton, M. S. I. Sarker, M. M. Rahman and M. K. R. Khan, Exploration of the structural, vibrational, electronic, mechanical and thermal properties of Ru₄Al₃B₂ and Ru₉Al₃B₈: a DFT study, *RSC Adv.*, 2023, **13**, 28912–28930.

76 D. L. Schodek, P. Ferreira and M. F. Ashby, *Nanomaterials, nanotechnologies and design: an introduction for engineers and architects*, Butterworth-Heinemann, 2009.

77 L. Sun, Y. Gao, B. Xiao, Y. Li and G. Wang, Anisotropic elastic and thermal properties of titanium borides by first-principles calculations, *J. Alloys Compd.*, 2013, **579**, 457–467.

78 O. L. Anderson, A simplified method for calculating the Debye temperature from elastic constants, *J. Phys. Chem. Solids*, 1963, **24**, 909–917.

79 M. E. Fine, L. D. Brown and H. L. Marcus, Elastic constants versus melting temperature in metals, *Scr. Metall.*, 1984, **18**, 951–956.

80 M. I. Naher and S. H. Naqib, An ab initio study on structural, elastic, electronic, bonding, thermal, and optical properties of topological Weyl semimetal TaX (X = P, As), *Sci. Rep.*, 2021, **11**, 5592.

81 M. F. Ashby, P. J. Ferreira and D. L. Schodek, Material classes, structure, and properties, *Nanomater., Nanotechnol. Des.*, 2009, **10**, 113–116.

82 D. R. Clarke, Materials selection guidelines for low thermal conductivity thermal barrier coatings, *Surf. Coatings Technol.*, 2003, **163**, 67–74.

83 Y. Liu, V. R. Cooper, B. Wang, H. Xiang, Q. Li, Y. Gao and B. Liu, Discovery of ABO₃ perovskites as thermal barrier coatings through high-throughput first principles calculations, *Mater. Res. Lett.*, 2019, **7**, 145–151.

84 G. A. Slack, The thermal conductivity of nonmetallic crystals, *Solid State Phys.*, 1979, **34**, 1–71.

85 C. L. Julian, Theory of heat conduction in rare-gas crystals, *Phys. Rev.*, 1965, **137**(1A), A128.

86 T. K. Ghosh, M. N. H. Liton, A. Chakraborty, M. K. R. Khan and M. S. I. Sarker, Atomic position dependent structural, electronic, mechanical and optical properties of ZnSbF₃ fluoroperovskites, *Mater. Sci. Semicond. Process.*, 2025, **187**, 109065, DOI: 10.1016/j.mssp.2024.109065.

87 A. Chakraborty, M. N. H. Liton, M. S. I. Sarker, M. M. Rahman and M. K. R. Khan, A comprehensive DFT evaluation of catalytic and optoelectronic properties of BaTiO₃ polymorphs, *Phys. B*, 2023, **648**, 414418, DOI: 10.1016/j.physb.2022.414418.

88 S. Li, R. Ahuja, M. W. Barsoum, P. Jena and B. Johansson, Optical properties of Ti₃SiC₂ and Ti₄AlN₃, *Appl. Phys. Lett.*, 2008, **92**(22), 221907, DOI: 10.1063/1.2938862.

89 M. Fox, *Optical properties of solids*, Oxford University Press, 2010, vol. 3.